OBSERVATIONS AND MEASUREMENTS OF TWO-PHASE FLOW PHENOMENA IN A WATER-COOLED REACTOR CAVITY COOLING SYSTEM DURING TRANSIENT SCENARIOS

A Thesis

by

DEMARKUS JERRELL HODGE

Submitted to the Office of Graduate and Professional Studies of
Texas A&M University
in partial fulfillment of the requirements for the degree of

MASTER OF SCIENCE

Chair of Committee, Yassin A. Hassan
Committee Members, Rodolfo Vaghetto
Kalyan Annamalai
Head of Department, Michael Nastasi

December 2019

Major Subject: Nuclear Engineering

ABSTRACT

The WRCCS is a cooling system in which the sole function is to remove heat from a VHTR, MSR reactor, or any reactor operating at high temperature. WRCCS was chosen for the experiment as opposed to an air-cooled reactor cavity cooling system. The research purpose was to observe two-phase flow and conduct measurements of temperature and flowrate during transient scenarios in the RCCS during two-phase flow. The WRCCS can operate in both single-phase during normal operations and two-phase when accident scenarios occur. Shakedown tests were performed prior to installing the optical sensor probe. Due to poor cross-correlation peak values, the probes could not be operated for the bubbly region. Once the determination was made the probes would not be included in as the main measurement of this experiment, high speed cameras were chosen instead. Consequently, high speed cameras were very effective and used as the main measurement device to track bubbles that were visible in the transparent glass upper manifold. In addition, temperature and flow rate were also measured to see the effects of two-phase flow in the WRCCS. Once bulk boiling was established in the WRCCS, there were instabilities in the two-phase flow. Inferences were made in this experiment that these instabilities caused changes in the flowrate of water, velocity of the bubbles, and temperature of the water. Lastly, changing the flowrate of water as dictated by the tank valve position, changed the two-phase phenomena during observation.

ACKNOWLEDGEMENTS

I would like to thank my committee members for supporting my research and allowing me to conduct two-phase measurements in the WRCCS. I would also like to thank Dr. Sero Yang for his assistance in solving problems that were associated with the experimental set-up.

CONTRIBUTORS AND FUNDING SOURCES

Contributors

This work was supported by a thesis committee consisting of Professor Yassin A. Hassan and Rodolfo Vaghetto of the Department of Nuclear Engineering and Professor Kalyan Annamalai of the Department of Mechanical Engineering. The data analysis for Chapter 7 was contributed to by Sero Yang. In addition, assistance with the experimental set up of the WRCCS facility was directly supported by David Holler of the Department of Nuclear Engineering. Also, Daniel Wacker is also recognized for helping with data post processing. All other work conducted for the thesis was completed by the student independently.

Funding Sources

Funding was for project NEUP Project N. 16-10245 by the U.S. Department of Energy.

NOMENCLATURE

APR	Advanced Power Reactor
FPS	Frames Per Second
ISO	Interface Software for Optical Probes
kW	Kilowatts
MELCOR	Methods for Estimation of Leakages and Consequences of Releases
MHTGR	Modular High Temperature Gas-Cooled Reactor
MSR	Molten Salt Reactor
NGNP	Next Generation Nuclear Plant
OSP	Optical Sensor Probe
PTV	Particle Tracking Velocimetry
RELAP5	Reactor Excursion and Leak Analysis Program
TTL	Transistor-Transistor Logic
UVP	Ultrasonic Velocity Profiles
V	Volts
VHTR	Very High Temperature Gas-Cooled Reactor
WRCCS	Water-Cooled Reactor Cavity Cooling System

TABLE OF CONTENTS

Page

LIST OF FIGURES

Page

LIST OF TABLES

Page

1. INTRODUCTION

A reactor cavity cooling system (RCCS) is a system that takes heat away from the core of a reactor. There are many reactors that have cooling systems in which an RCCS is applicable. For example, light water reactors, gas-cooled reactors, molten salt reactors, and liquid metal reactors can take advantage of the RCCS cooling. There are 2 types of RCCS, an air-cooled RCCS and a water-cooled RCCS. The air-cooled RCCS can only operate under single phase, while the water-cooled RCCS can operate in both single and two-phase conditions.

When operating a reactor, there are many factors that can cause the temperature of the core to increase. Usually when taking out the control rod, the reactivity of the core increases directly causing an increase in temperature. In normal operation of the reactor, the RCCS will continue to operate as the temperature fluctuates. For the air-cooled RCCS system, the *Modeling and Performance of the MHTGR Reactor Cavity Cooling System* (Conklin, 1990) states, “"The RCCS uses natural convection as a method to induce air flow through the panels and ducts of the system to cool the nuclear core inside an uninsulated reactor vessel. The buoyant forces in the system are induced by a density difference between the heated air inside the system and the ambient air. No active components or moving parts are used in the design.” Moreover, the water-cooled RCCS uses natural convection to drive the flow of water; therefore, forced convection is not necessary. The water exchanges heat with the core of the reactor to reduce the temperature of the reactor. Figure 1.1 shows the RCCS cooling system usage via a reactor.

Having a cooling system is necessary for reactors, especially when an accident scenario occurs. For instance, as the reactor core approaches super critical, the core temperature begins to increase. During accident scenarios, the water-cooled RCCS can establish two-phase conditions.

The void fraction of the two-phase is a parameter that allows engineers to understand and quantify the amount of gas present in the gas-phase and in the control volume. Observing the two-phase phenomena is vital to the progression of computational fluid dynamics of two-phase flow. Likewise, to ensure progression of computational fluid dynamics further, empirical data from experimentation is necessary for accurate simulation. Therefore, observing two-phase flow in the water-cooled RCCS is an important step to the development of empirical correlations that will allow for more accurate simulations in transient scenarios.

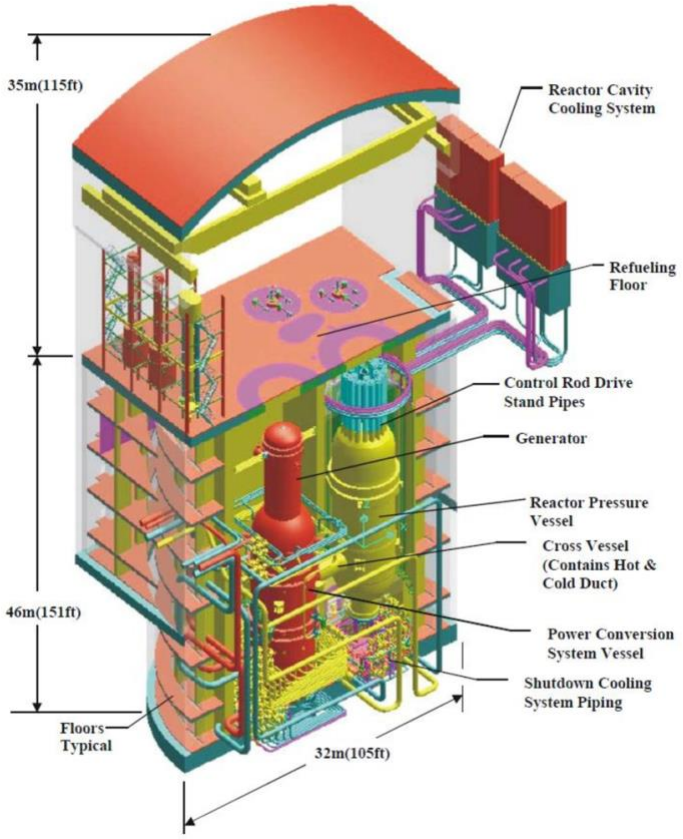

Figure 1.1: Reactor Cavity Cooling System (Hassan, 2013)

2. LITERATURE REVIEW

Researchers have studied water-cooled reactor cavity cooling systems (WRCCS) to develop a body of work in which future researchers can build upon. Unfortunately, not enough research was done; however, this body of work continues to increase. Although research is limited on WRCCS, most of the WRCCS work conducted was in a single-phase application, and only a small amount of research has been conducted for two-phase flow in a WRCCS. For single-phase applications of the WRCCS, a research article entitled, "*Water-Cooled Reactor Cavity Cooling System Flow Analysi*s" by Casey Tompkins & Michael Corradini was reviewed. In this research, a ¼ scale of the WRCCS facility with 3 risers was observed. A WRCCS facility with 3 risers allowed a flow analysis to be conducted. As the single-phased application of the WRCCS facility used water as the coolant liquid, the flow was driven by natural circulation. Additionally, this experiment was conducted at steady state in order to analyze the flow behavior when the WRCCS was in operation. Researchers concluded that when the WRCCS operated in single phase, the flowrate was stable. In addition, the single-phase losses were directly proportional to the mass flowrate (Tompkins & Corradini, 2018).

In the article, "*Experimental and Computational Study of a Scaled Reactor"* by Rodolfo Vaghetto in 2013 the study of a WRCCS in which the facility was scaled down was conducted. The researchers also evaluated a specific design and build for trends. In this study, there were 9 risers at 1/23 which was the scale of the actual facility. The researcher collected data and steady state measurements. RELAP5 simulations were conducted for the steady state. Results showed that the WRCCS can be operated at steady state conditions in which the RELAP5 simulations agreed with the experimental results (Vaghetto, 2013).

Not only was the single phase WRCCS researched, but the two-phase applications as well. This was important because when there was an accident, the reactor temperature in the WRCCS could establish a flow which showed both the liquid and gas phases of water were present simultaneously. When comparing two-phase flow research, the lack of available WRCCS research made it difficult to compare. This was identified as a limitation of this literature review. In the next article, *"Two-Phase Natural Circulation Flow of Air and Water in a Reactor Cavity Model Under an External Vessel Cooling During a Severe Accident"* by Park and colleagues, two-phase cooling applications were explored. In this application, the researchers simulated an Advanced Power Reactor (APR) in which an external reactor vessel cooling was used. The external reactor vessel cooling in this study used water as the cooling fluid. The experiment also showed how RELAP5 was used to simulate the external vessel cooling during a severe accident. The results demonstrated the external reactor vessel established two-phase flow. By simulating the injection of air into the external reactor vessel, two-phase flow simulation occurred. Finally, the results showed a correlation between the increase of water in the inlet area and the water level in the reactor cavity. This led to an increase in the water circulation mass flow rate (Park et al., 2006).

Another article was reviewed called, "*Influenced of Boil-Off on the Behavior of a Two-Phase Natural Circulation Loop" by* Lisowski and colleagues. Using a ¼ scale of the WRCCS with three risers in a two-phase test, research was conducted in which the facility was heated. In this test, five different natural circulation flows were identified, which consisted of a single-phase heating, transitional nucleate boiling, hydrostatic head fluctuations, stable two-phase, and geysering. As the water evaporated and the water level was reduced, it caused a shift in the boiling boundary of different segments of the loop. As the water level continued to reduce, a

break in the loop occurred which induced flow stagnation with the geysering effect in the heated region. At this point, there was a decrease in the heat removal process the WRCCS provided, which could have potentially caused a burn out and damage to the WRCCS facility. In this scenario, the article showed how venting the steam could cause an increase in heat removal times. This was significant because it would allow for two-phase flow to be sustained longer in the WRCCS (Lisowski et al., 2013)

The article, *"Flow Pattern Transition Instabilities in a Natural Circulation Cooling Facility by* Casey Tompkins and Michael Corradini documented the research using another ¼ scale of the WRCCS with three risers in a two-phase test was conducted as the facility was heated. Researchers measured pressure drop and mass flow rate to observe the effects during both single-phase and two-phase testing. Researchers concluded as the WRCCS established two-phase flow, the differential pressure was decreased when compared to single-phase flow (Tompkins, & Corradini, 2018).

"A Study Using RELAP5 on Capability and Instability of Two-Phase Natural Circulation Flow Under Passive External Reactor Vessel Cooling" by Zhao Gouzhi, Cao Xinrong, & Shi Xingwei was the next research article reviewed. In this study, a simulation using RELAP5 reactor vessel demonstrated how the reactor generated heat. At the end of the simulation, an external reactor vessel cooling two-phase flow was established. In this external reactor vessel cooling, the flow was driven by natural circulation. After running the simulation, it was reported that two-phase flow was prevalent during the early stages. It was also determined that steady two-phase natural circulation flow could not be established, and an intensive flow rate oscillation and back flow occurred as the flooding water sub cooling fell below the critical value (Gouzhi, Xinrong, & Xingwei, 2013).

In the article, "*Experimental Investigations in a Reactor Cavity Cooling System with Advanced Instrumentation for the study of Instabilities, Oscillations, and Transients"* by Rodolfo Vaghetto, & Yassin A. Hassan, these researchers used a ¼ scale of the WRCCS with 3 risers in their facility. Once the WRCCS was heated, temperature, pressure, and void fraction were measured. Using MELCOR modeling, WRCCS system performance and stability were predicted. In this model, mass flowrate oscillations were predicted both small and large. In addition, void fraction was measured using an RBI probe in each of the three risers, and in the tank. The significant of this study was because void fraction was measured in all three raisers, and thus allowing void fraction to be compared against flowrate, temperature, and pressure. Researchers concluded two-phase measurements can be conducted, and the two-phase flow is unstable. Lastly, researchers observed oscillations in the flow (Vaghetto, & Hassan, 2014).

The article, "*Experimental Studies of NGNP (Next Generation Nuclear Plant) Reactor Cavity Cooling System with Water*" by Casey Tompkins & Michael Corradini described a ¼ scale of a WRCCS. This research study the WRCCS flow. In this application, the study of temperature, pressure, and flowrate was analyzed. Ultrasonic velocity profiles (UVP) instrument was used to obtain velocity profiles in all 3 risers. An optical sensor probe was used to determine the void fraction once the facility water reached saturation temperature in the tank inlet. A dual tip probe was used with sapphire tips and was installed in the tank. In this study, single-phase and two-phase applications were also explored. Researchers concluded in two-phase flow in the WRCCS, the bubbles expand when rising through unheated portions. Finally, researchers detected flashing instability when the vapor was produced first in the headed section in the case of geysering. Flashing vapor was formed by the decrease in hydrostatic head as the water flowed upward (Tompkins & Corradini, 2018).

Various research has been accomplished pertaining to single-phase WRCCS. As such, researchers can obtain more data, which leads to a better understanding of flow behavior, differential pressure, and temperature distribution. In addition, some research has also been done in two-phase WRCCS with a ¼ scale that contains three risers. However, there has been no experimental studies that involve two-phase flow in a 1/23 scale with 9 risers. Since it is important to understand the flow behavior changes when more risers are added and the height the risers change, more research studies must be conducted using two-phase flow in a 1/23 scale with 9 risers. Understanding the effects of having more risers will allow for computational simulations to have a more accurate simulation when modeling a full scale WRCCS. One reason two-phase flow has very limited research done with a WRCCS is due to minimal working WRCCS experimental facilities. Most WRCCS facilities have steel upper and lower manifolds attached to the riser panels which makes it impossible to observe the two-phase phenomena in the type of riser panel. Based on the literature review, researchers in this study found the WRCCS at Texas A&M University contains the only WRCCS with glass transparent upper and lower manifolds. In conclusion, Texas A&M University's observations of the two-phase flow phenomena in the WRCCS with 9 risers will be conducted for the first time.

3. SCOPE

The scope of this study was to observe the two-phase flow in the riser panel, and conduct measurements of the temperature during transient scenarios. The bubble size and velocity in the risers were evaluated during transient time periods. Lastly, characterizations of the two-phase flow behavior with temperature behavior during transient conditions were studied as well. As such, the purpose of this research is to observe two-phase flow and conduct measurements of temperature and flowrate during transient scenarios in the RCCS during two-phase flow.

4. FACILITY DESCRIPTION

In the RCCS, there is a reactor cavity as illustrated in Figure 4.1. This reactor cavity contains nine risers, three 8kW heaters operating at 38% of the total power, and an upper and lower manifold. The upper and lower manifold are constructed out of glass and are transparent, while the risers are constructed out of steel. In addition, there is a hot leg of steel piping that is connected to a water tank 20 ft above the glass upper manifold. Then, a cold leg or down comer connects the water tank to the inlet of the riser panel. After a cooling system was installed, it kept the RCCS operating at steady state. The cooling system contained a water chiller that was connected to the water tank by pipes and a heat exchanger. The pipes were designed to carry water to the heat exchanger in order to take away heat in the tank to keep the RCCS operating at steady state.

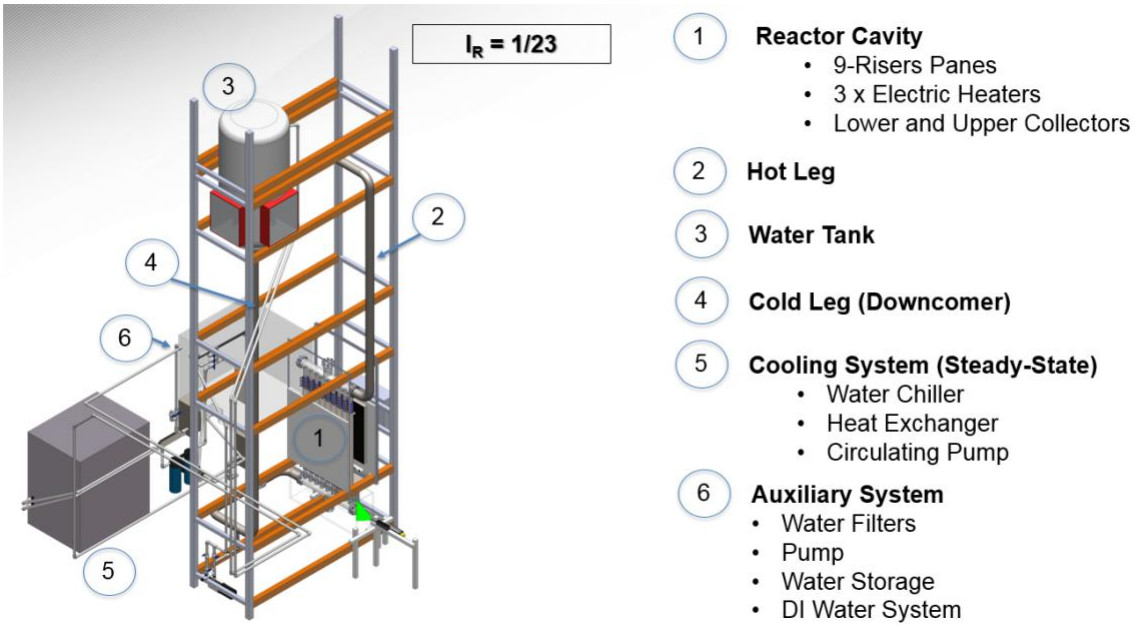

Figure 4.1: Facility Overview

The reactor cavity is the primary focus in this study. Figure 4.2 depicts the reactor cavity. The main points of observation will be in the transparent glass upper manifold to see the two-phase phenomena. In addition, it can be seen that the three 8kW heaters are heating the front of the panel and water flow upward past the heaters to carry the heat to the outlet of the riser panel. Furthermore, a magnetic flow meter is placed at the inlet of the riser panel to monitor any flow changes of the water.

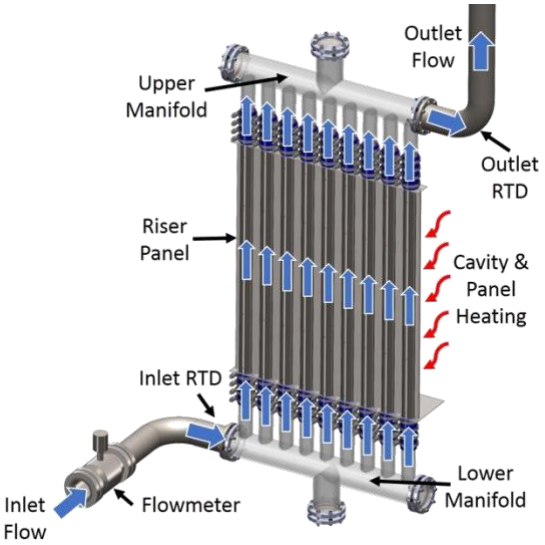

Figure 4.2: Reactor Cavity

The riser panel is constructed out of steel. The inner diameter of the risers is 2 inches, and the fins are connected to the risers. There is a total of 137 K-type thermocouples. Eighty-five of the thermocouples are dedicated to wall measurements both on the fins and the risers. In Figure 4.4, thermocouples on the wall and water probes are showed. Also, there are 52 water probes in the risers of the riser panel to take water measurements.

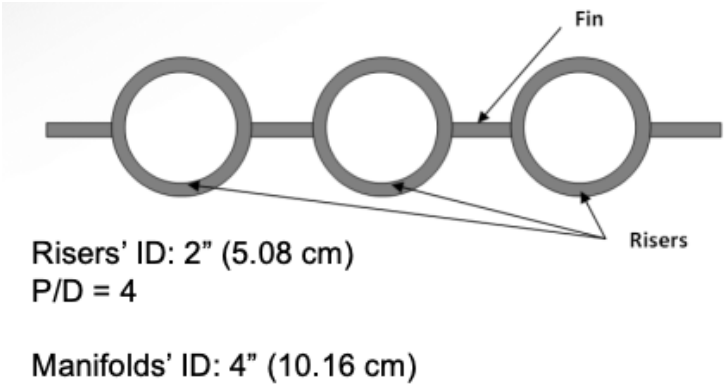

Figure 4.3: Risers and Fins on the Riser Panel

Figure 4.4: Riser Panel with Thermocouples Installed on the Walls and Water Probes

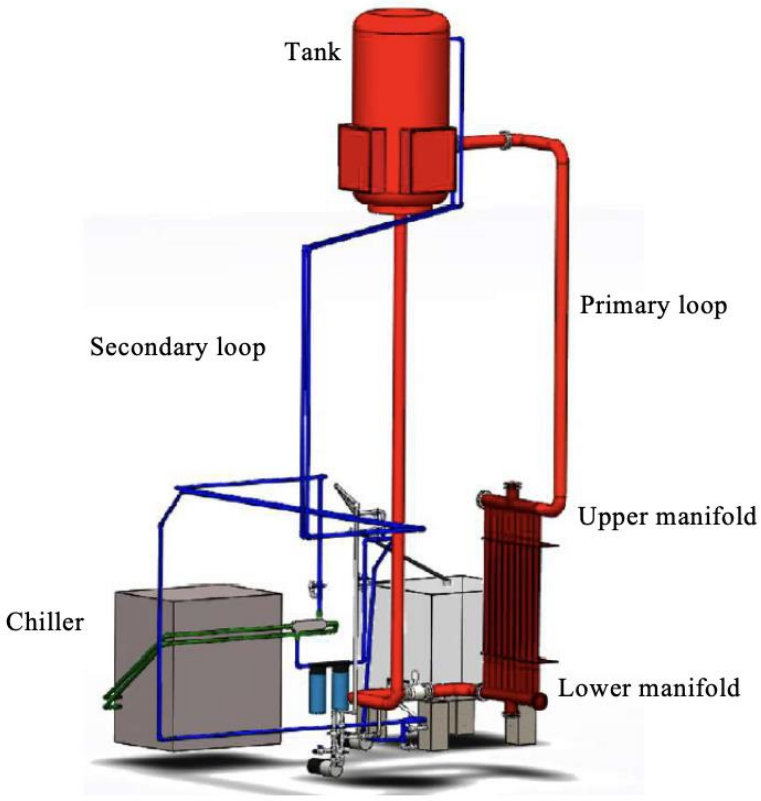

Figure 4.5: WRCCS Facility with the Red Loop Being the Primary Loop and the Blue Being the Secondary Cooling Loop

The facility uses natural circulation that allows the water to flow from the lower manifold to the upper manifold. Using the primary loop (Figure 4.5), the water flows upward to the tank. Once the water reaches the tank, it continues to flow downward to the lower manifold using the primary loop. In the secondary loop (Figure 4.5), water flows from the chiller to the top of the tank using a pump. This secondary water loop is connected to the primary loop through a heat exchanger that allows heat to transfer to the secondary loop, thus increasing the temperature of the secondary loop. Using the chillier substance, the heat is removed from the secondary loop to reduce the temperature of the secondary loop. Figure 4.2 is a more detailed view of the riser panel. The water flows into the inlet of the riser panel to the lower transparent glass manifold.

Next, the water flows upward through the riser panel to the transparent glass upper manifold. Once in the upper manifold, the water flows out the outlet to the water tank.

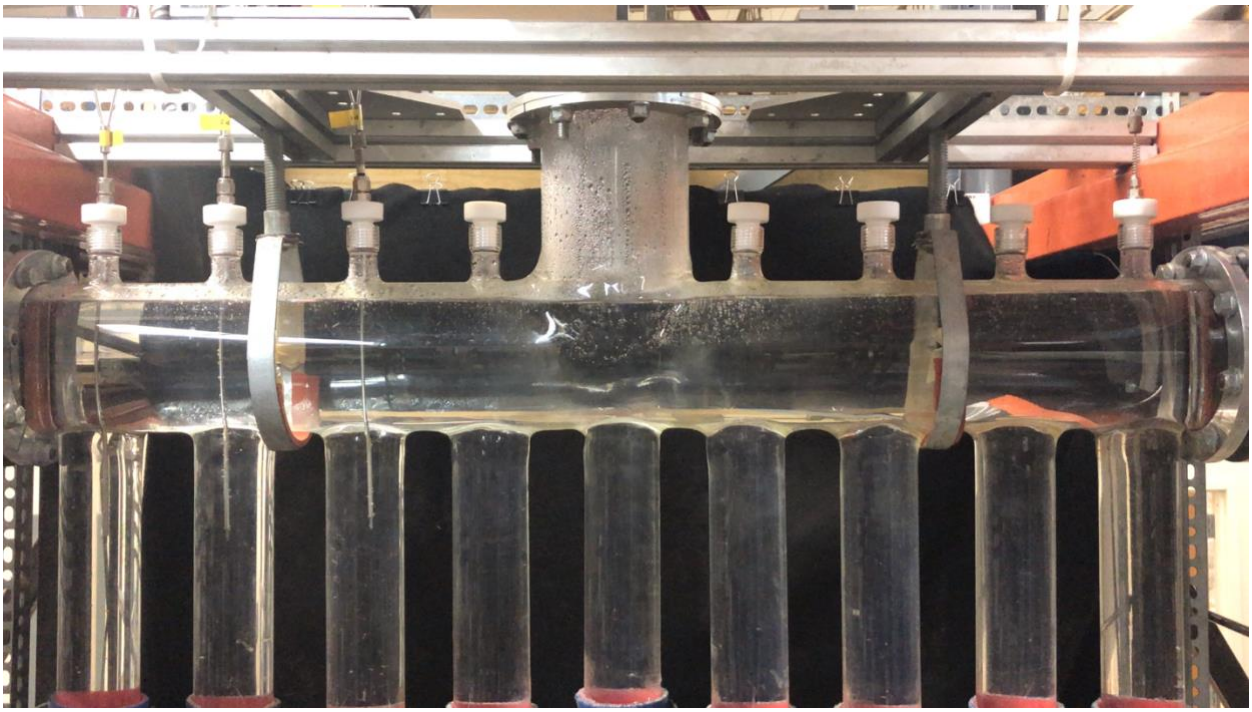

Figure 4.6: Top Glass Manifold with Optical Probes Installed on Riser 1, 2, and 3

In this experiment, three probes were installed on a glass manifold (Figure 4.6), which is connected to 9 steel risers. This is further connected to the riser that contains another glass manifold located at the bottom of the riser, which is in an inverse position than the glass manifold located at the top. Inside these steel risers and glass manifolds, there is water that is heated indirectly by three 8 kW heaters operated at 33% of the total power. The flow is entirely driven by natural circulation, and the water flows upwards towards a tank that is 20 ft above the glass manifold. The water first intersects the sapphire tips and continues to flow upward.

5. INSTRUMENTATION

5.1. Type-K Thermocouples

There are 45 thermocouples which are placed on the riser panel (Figure 5.1). Each of the 9 risers have 5 positions in which the thermocouples measure the water of the riser panel. In addition to the 45 thermocouples placed on the riser panel, there are 2 additional thermocouples, one at the inlet of the risers and one at the outlet of the riser panel. Also, there are 87 thermocouples that measure wall temperatures of the risers and the fins.

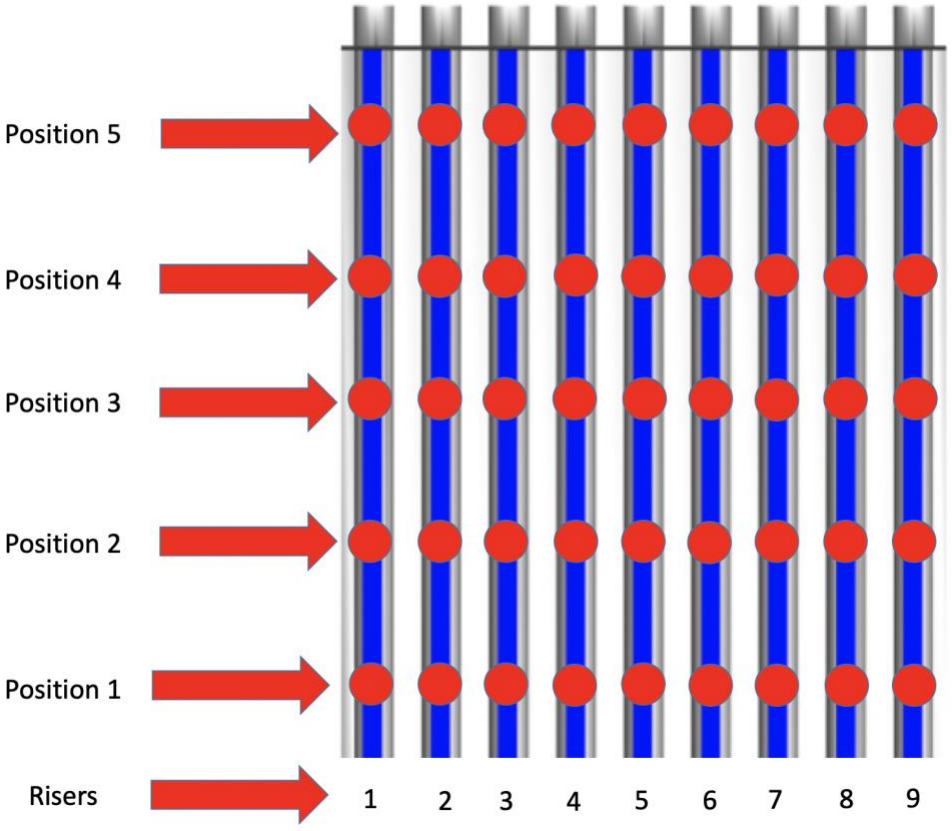

Figure 5.1: Thermocouples Positions on the Riser Panel

Each thermocouple for the wall and the water were calibrated by placing the thermocouples in the room temperature insulating the thermocouples (Figure 5.2 a). Using a fluke meter, the temperature inside the insulation at room temperature was measured to get an accurate temperature. The type k thermocouples were placed in the room temperature insulation for 12 hours to get an accurate measurement of temperature using the uncalibrated type k thermocouples. After that, the thermocouples were placed in boiling water using a pot as seen in Figure 5.2 b to heat up the water. The fluke meter was used to accurately get a measurement of temperature for the boiling water to get a measurement for the saturation temperature in atmospheric pressure. The uncalibrated type k thermocouples were placed in the pot for a 2-hour duration for accurate temperature measurements. In addition, the thermocouples were placed in an oven (Figure 5.2 c) to get the uncalibrated thermocouple measurement for an intermediate temperature for 2 hours. Using the correct temperatures from the fluke meter, the uncalibrated type-k thermocouples points were adjusted to the correct temperatures using LabVIEW VI. This temperature adjustment was completed by calculating a slope and using the two correct temperatures to make an equation for the line. Due to the size of the pot for getting the boiling temperature of the calibration, the thermocouples were calibrated in three batches. Although these temperatures were measured, the wall temperature measurements were not in the scope of this study.

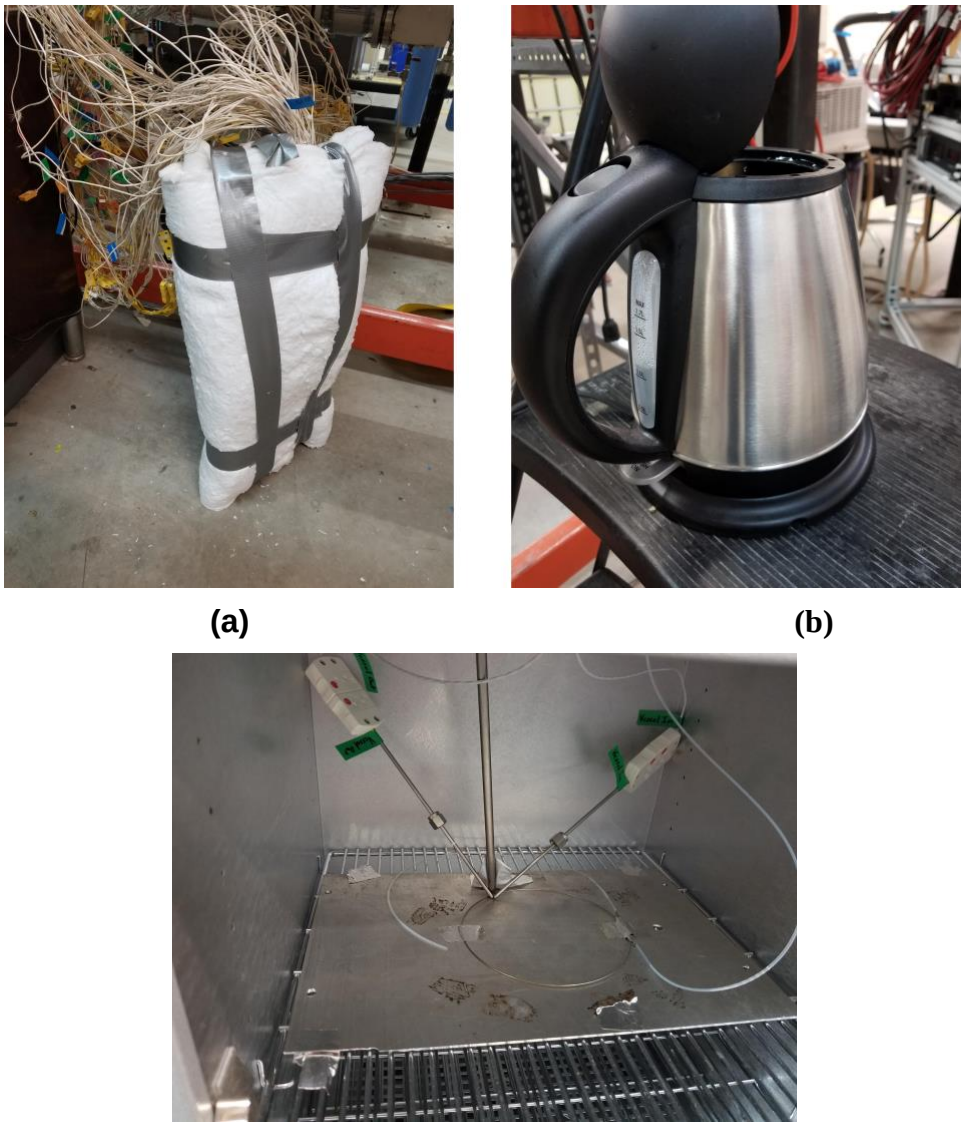

Figure 5.2: Equipment Used to Obtain Room Temperature (a), Saturation (b), and Intermediate / Over 100 C (c) Calibration Points.

5.2. Magnetic Flowmeter

Moreover, a flowmeter was used to measure the flowrate of water at the inlet of the riser panel. The magnetic flowmeter measured flowrate by applying a voltage across the fluid and measuring the potential difference across the fluid. This potential difference is proportional to the flowrate of the water. In Figure 5.3, this can be seen. The magnetic flowmeter was placed at the inlet and connected to the lower riser panel. The flowmeter was placed in this location to measure the changes in flow of water as the riser panel was heated by the three 8 kW heaters.

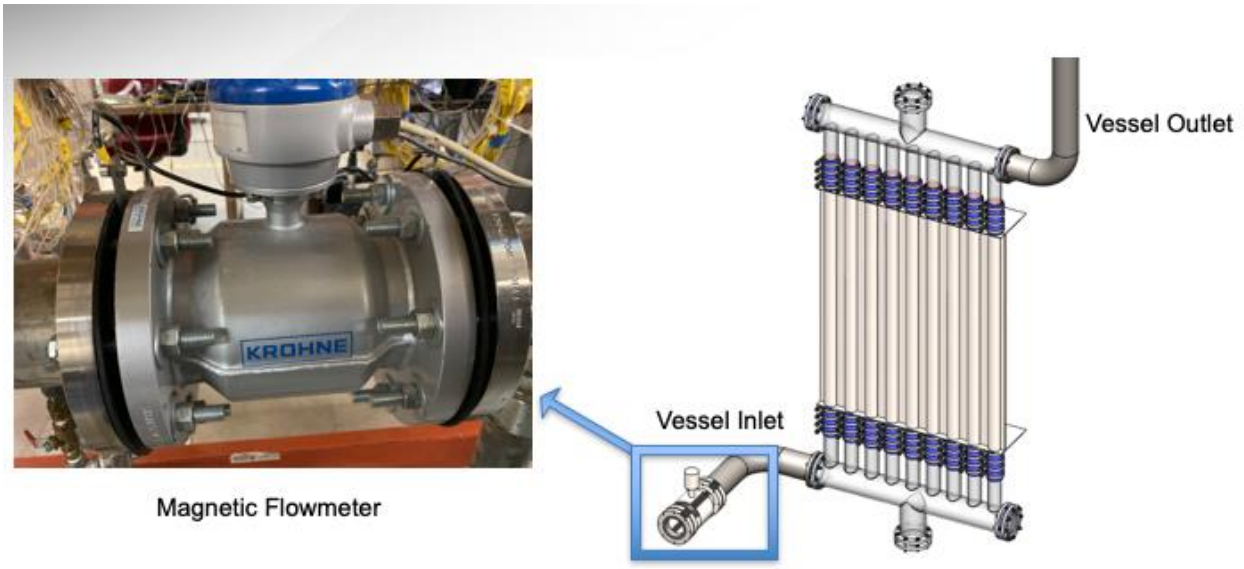

Figure 5.3: Magnetic Flowmeter Installed at the Inlet of the Riser Panel

5.3. Two-Phase Optical Probes

The main measurement component is the optical sensor probe as shown in Figure 5.4. This is used for void fraction and velocity measurements. The probe is constructed of two sapphire tips that are attached to an optical fiber as seen in Figure 5.4. The fiber is protected by steel piping. The sapphire tips (Figure 5.5 b) measured the index of refraction in a liquid or gas. Next, the e parameter which is associated with the corresponding probe represented the distance between the sapphire tips. This e parameter was used in the geometry and location section of the ISO software in the probe geometry and location section of the ISO software. Table 5.1 shows each probe used with the corresponding e parameter and with the corresponding sensor in probe geometry.

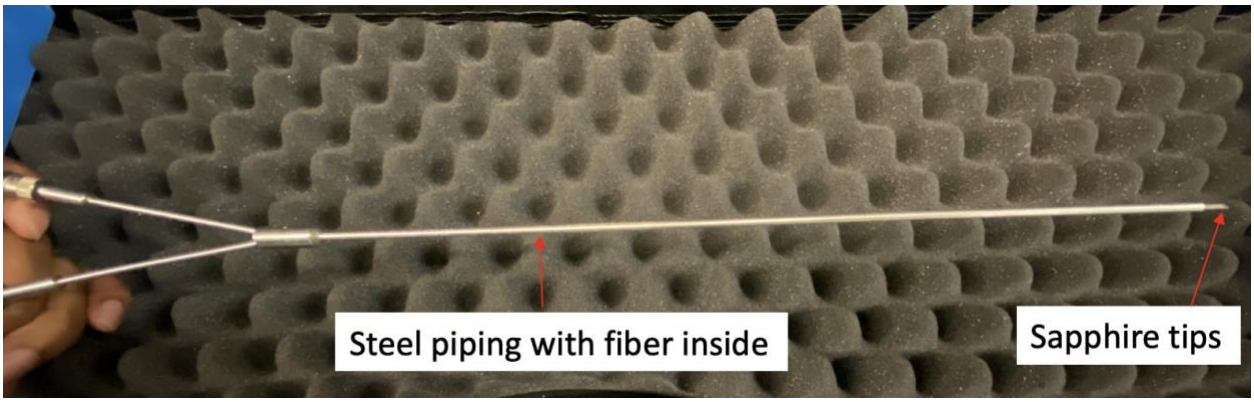

Figure 5.4: Optical Sensor Probe

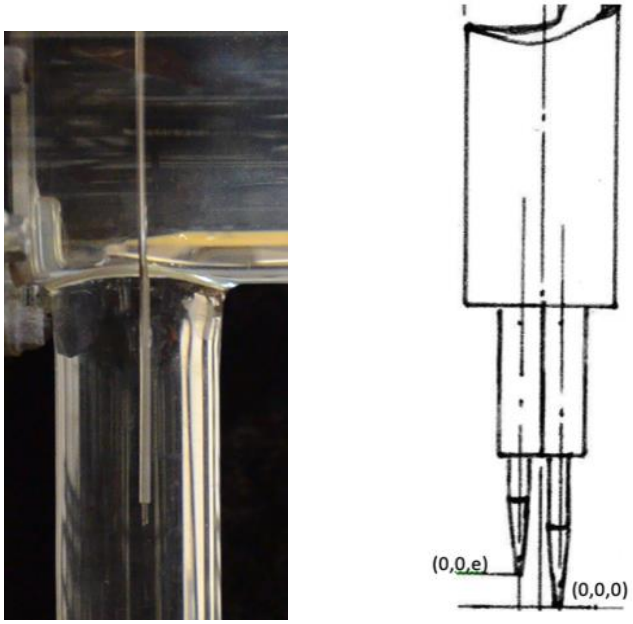

(a) (b)

Figure 5.5: (a) Zoomed in Optical Sensor Probe. (b) Coordinates of Each Sensor Input into the ISO Software

Table 5.1: Probe with Corresponding e Parameter and Sensor in Probe Geometry

Probe	e	Sensor
1	0.8	4 and 5
2	0.6	2 and 3
3	0.65	0 and 1

The oscilloscope (Figure 5.6a) is used to display the signal from the opto-electronic unit The opto-electronic unit (Figure 5.6c) is an amplifier that is able to shape and amplify the signal received by the probes. Once the signal is appropriately manipulated, the signal is then sent to the acquisition module (Figure 5.6b). The acquisition module converts the signal to a digital format the ISO software can understand in order to perform the correct calculations. Figure 5.7

shows how the oscilloscope, acquisition module, and opto-electronic unit function. Table 5.2 contains a list of all the probe equipment that is used when operating the probe.

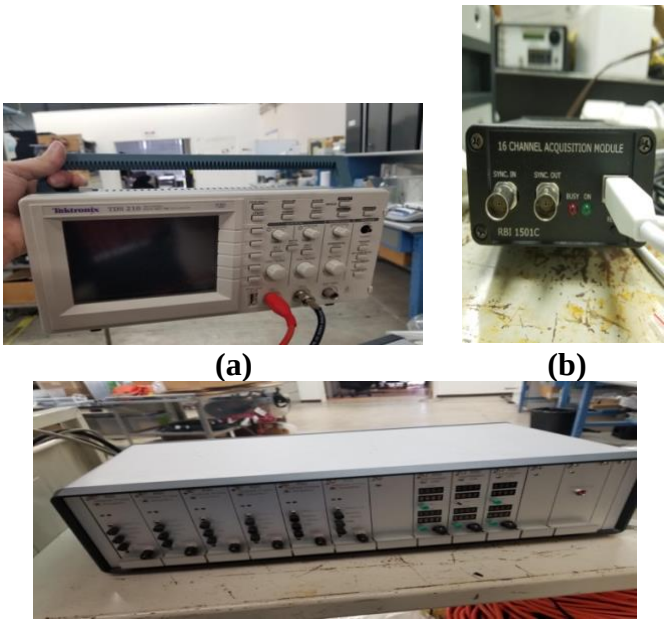

(a) **(b)**

(c)

Figure 5.6: (a) Oscilloscope (b) Acquisition Module (c) Opto-Electronic Unit

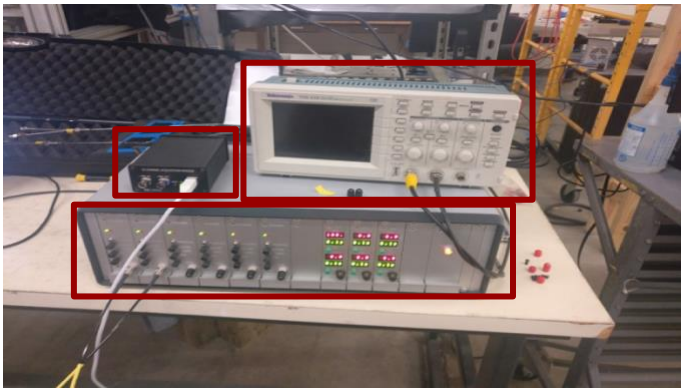

Figure 5.7: Oscilloscope, Acquisition Module, and Opto-Electronic Unit Connected and Operating

Table 5.2: Components of Equipment Used to Measure the Void Fraction of Liquid

Optical Probe 1 (P1)*	Calibration	e = 0, 80
Optical Probe 2 (P2)*		e = 0, 60
Optical Probe 3 (P3)*		e = 0, 65
Oscilloscope	Voltage Output Signal Visualization Purposes	
	Model Number	Tektronix TDS 210
	Serial Number	B071109
Acquisition Module	For ISO Software to Obtain the Data from Optical Probe Amplifiers	
	Equipment Number	RBI 1501C
Opto-Electronic Unit Containing Optical Probe Amplifiers	Optical probe amplifiers are for adjusting the signals they receive from the optical probe. There are a total of six amplifiers that are included in the unit.	
Cordon fibre HCL 400	RCSPE-RBI17	113-6

*The Optical Probe Contains the Optical Fiber Protected by a Stainless Tube.

5.4. High-speed Cameras

Phantom Miro high-speed cameras were placed in front of the transparent glass upper manifold in order to view the two-phase phenomena. Holding the cameras in place is a traverse system that allows for vertical movement of the cameras for viewing angle adjustments. Each camera had a view of 3 risers to capture all 9 risers. Figure 5.8 displays the placement of the cameras in front of the transparent risers as well as the light panel. The light panel was used to give more light exposure to the lens to clearly view the bubbles in the transparent glass upper manifold. Also, a 50 mm lens was used to view the 3 risers in a single camera view. Having a 50 mm lens allowed for all 9 risers to be captured using three cameras. Once the cameras were installed and the viewing angles were made optimal, the camera speed was determined. After observing a cycle when the water started boiling in the RCCS, it was determined the time duration of the cycle was 30 seconds. This meant that the cameras had to capture a cycle in a single recording. After clearing the 120 gigabyte memory and setting the framerate of the cameras to 240 fps, all three cameras were able to record for 34 seconds. Also, Figure 5.9 shows the cameras placed directly in front of the transparent risers.

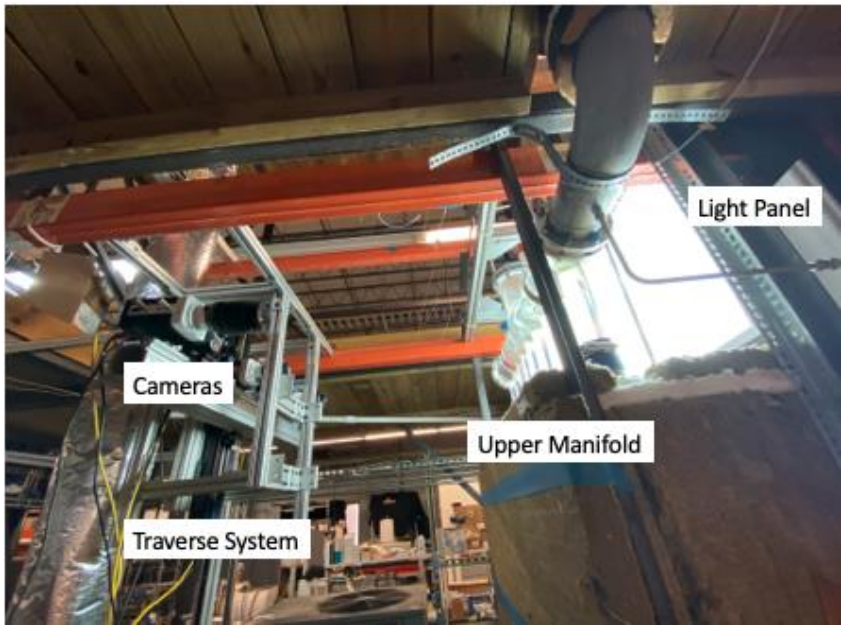

Figure 5.8: Three Cameras Placed in Front of the Transparent Risers

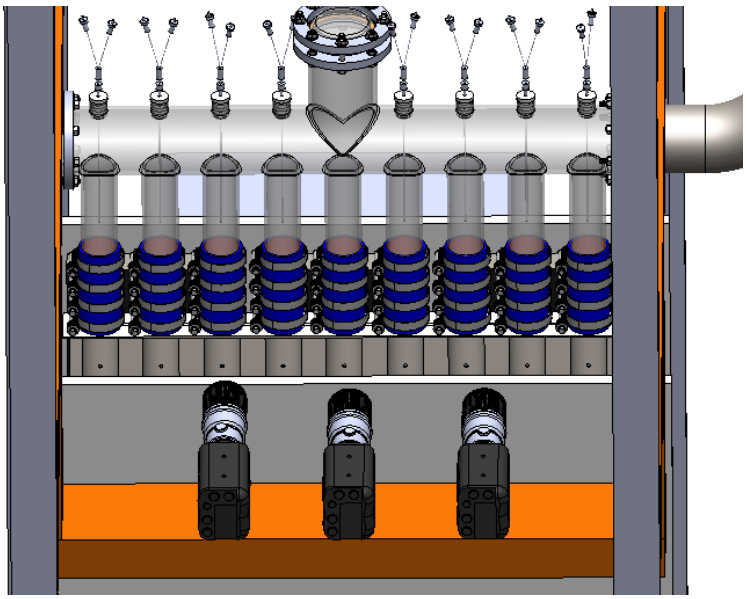

Figure 5.9: Three Cameras Placed in Front of the Transparent Risers.

6. WORKING PRINCIPLE OF OPTICAL SENSOR PROBE EQUIPMENT

6.1. Working Principle of the Optical Sensor Probes

Phase discrimination with an optical probe rests on the discrete variation of the refraction index between the various flow components. The optical probe sensitive area (see Figure 6.1) acts as a Descartes prism. This phenomenal depends on the refraction index of the medium in contact with the prism and on the angle of incidence of the ray of light. The ray is either reflected or diffracted by the wall.

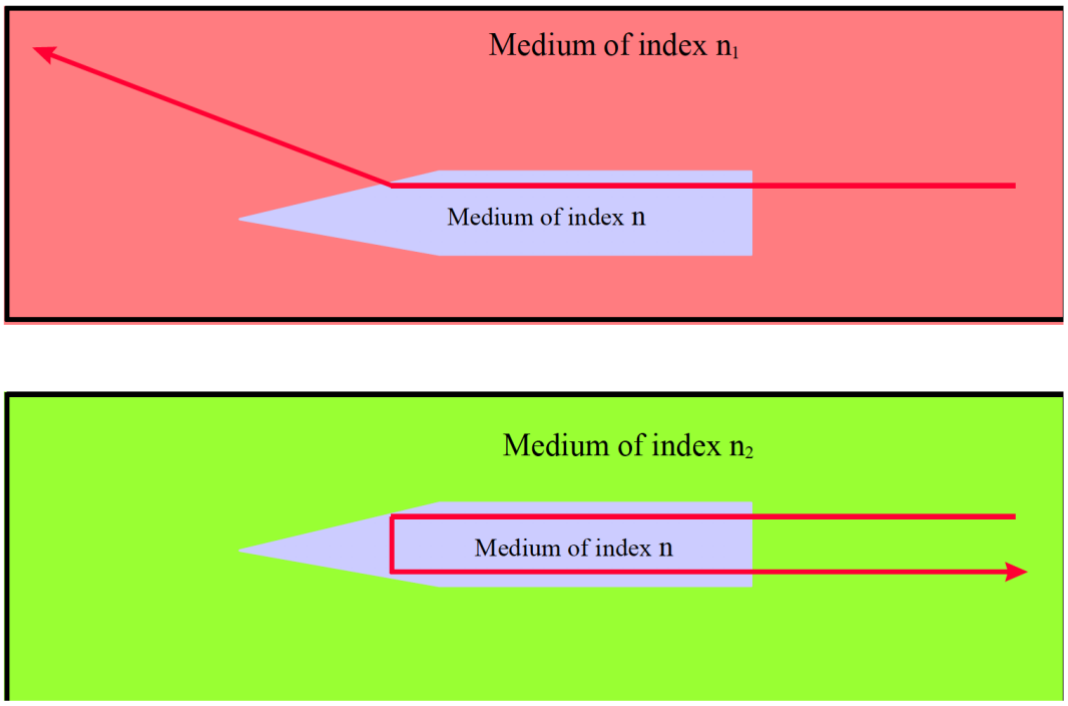

Figure 6.1: Optical Probe Principle (RBI, 2005)

At a given emission of light, the quantity of light reflected by the wall of an optical probe sensitive tip depends exclusively on the refraction index of the medium external to the wall. The

conversion of the optical signal (quantity of light reflected) into an electrical signal is ensured by a photo-sensitive element.

Using light, response times are short and insignificant versus those of the probes operating on the electrical properties of the materials (resistive and capacitive probes). The small dimensions of the sensitive areas, a few microns wide (whatever the type of tip: sapphire or drawn optical fiber), can impact response time as well. It should be remembered the sensitive areas of a hot wire, although constituted by a conducting wire a few microns in diameter, are characterized by dimensions in millimeters.

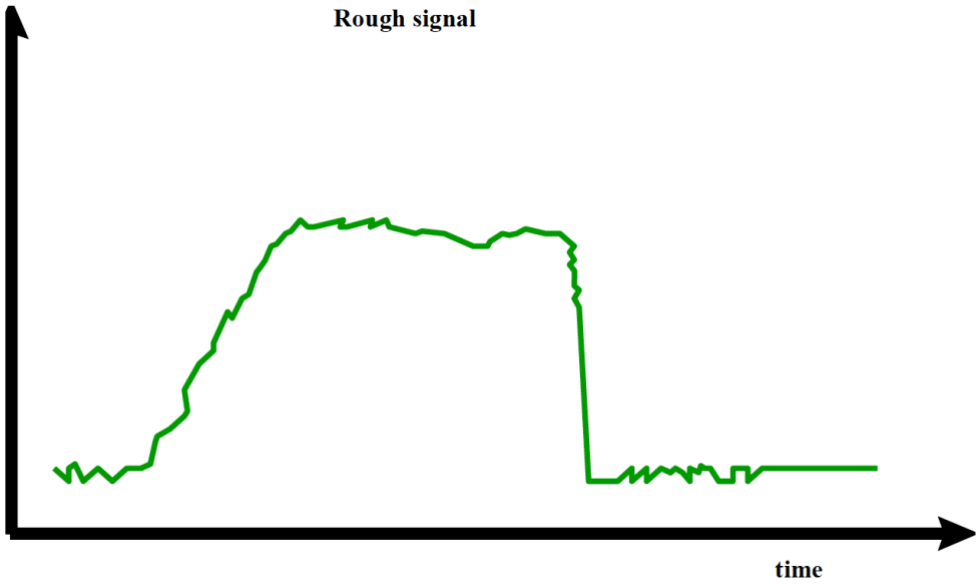

Figure 6.2: Production of a Shaped Signal (RBI, 2005)

As shown in Figure 6.2, when a bubble goes through the tips, the optical probe produces a variable level analog signal via its transmission reception transformation module. The probes are very sensitive to movement. Moving the cables can cause a change in the output signal that

can be viewed using the oscilloscope. In addition to movement of the cables, the signal will vary as the temperature of the water increases causing a change in the output signal. Also, the sapphire tips on the probe have to come into contact with the bubbles by both tips to receive two signals to calculate the velocity using the e parameter associated with each probe. This can become extremely challenging due to the random nature of bubble formation or vapor production.

6.2. Optical Sensor Probe Installation

The equipment needed to install the probes are the plug adaptor, the metal fitting enclosure, and the plastic fittings. Figure 6.3 shows the plug adaptor and Figure 6.4 shows the metal fitting enclosure and the plastic fitting.

Figure 6.3: Plug Adaptor

Figure 6.4: Metal Fitting Enclosure (Left) and Plastic Fitting Enclosure (Right)

The first step is to secure the plug adaptor to prevent it from moving vertically or axially. Next, confirm the plug adaptor is leveled so the drill bit cuts the plug adaptor straight as seen in Figure 6.5. This will ensure the probe is straight when taking measurements.

Figure 6.5: Plug Adaptor Leveled Before Drilling

Using a 1/8 drill bit, drill through the entire plug adaptor at the center. This hole will act as a guide for the 3/16 drill bit. After that, using a 3/16 drill bit, drill through the entire plug adaptor at the center. Figure 10.6 shows how the 1/8 drill bit is used, and Figure 6.7 shows how the 3/16 drill bit is used for the construction of the plug adaptor.

Figure 6.6: Drilling Through the Plug Adaptor with a 1/8 Drill Bit

Figure 6.7: Drilling Through the Plug Adaptor with a 3/16 Drill Bit

Using an 11/32 drill bit, drill 1 cm into the plug adaptor at the center from the top. This hole will act as a guide for the 3/8 drill bit. After that, using a 3/8 drill bit, drill 1 cm into the plug adaptor at the center from the top. Figure 6.8 shows how the 3/8 drill bit is used for the construction of the plug adaptor. Before making the treads for screwing on the fitting enclosure, level the plug adaptor again to ensure the threads are cut straight to ensure the probe is straight. Using a 1/8 tap, slowly twist the tap until the treads are cut 1 cm into the plug adaptor from the top. Figure 6.9 shows how the 1/8 tap is used to cut the groves for the metal fitting enclosure to screw in the plug adaptor to create a tight seal.

Figure 6.8: Drilling Through the Plug Adaptor with a 3/8 Drill Bit

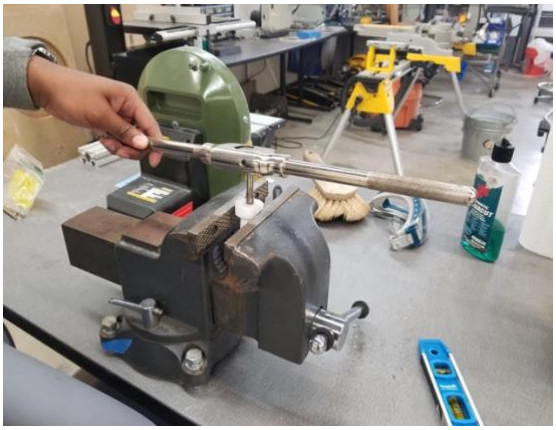

Figure 6.9: Tapping the Plug Adaptor with a 1/8 Tap

Take the top of the metal fitting enclosure and slide it onto the probe. Next, slide the plastic fittings onto the probe. In addition, slide the end of the metal fitting enclosure on the probe, and twist the top and bottom together so that the fitting enclosure is secure and does not move along the probe. When done, slide the plug adaptor on the probe (Figure 6.10) and screw the plug adaptor to the fitting enclosure. Finally, place the probe in the WRCCS, and screw the plug adaptor in the top manifold of the WRCCS. Figure 6.11 demonstrates how the sensor is installed into the WRCCS

Figure 6.10: Optical Sensor Probe

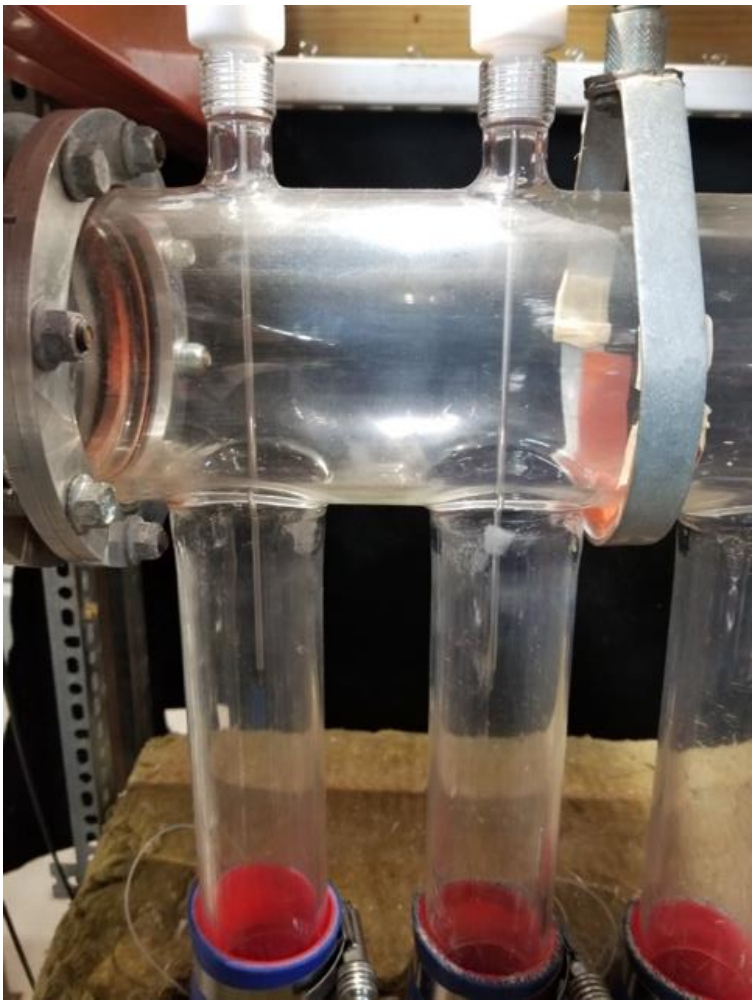

Figure 6.11: Optical Sensor Probe Installed on the WRCCS

6.3. Optical Sensor Probe Calibration

6.3.1 Initialization of the Gain and the Zero

Place the gain switch on the lowest position (downwards). Adjust the coarse anticlockwise up to the extremity. Figure 6.12 shows the course, fine, and gain potentiometer switches.

Figure 6.12: Course, Fine, and Gain Potentiometer Switches

6.3.2 Adjust of the Optimum Emission Current

Connect the probe onto the opto-electric unit, and leave the tip of the probe (sapphire tip) in the air. Using a 2mm diameter flathead screwdriver, search for the extinction threshold level of the green light. Logically, this light is switched on. Turn the potentiometer clockwise until the light switches off. To switch it on again, turn the screw slightly anticlockwise.

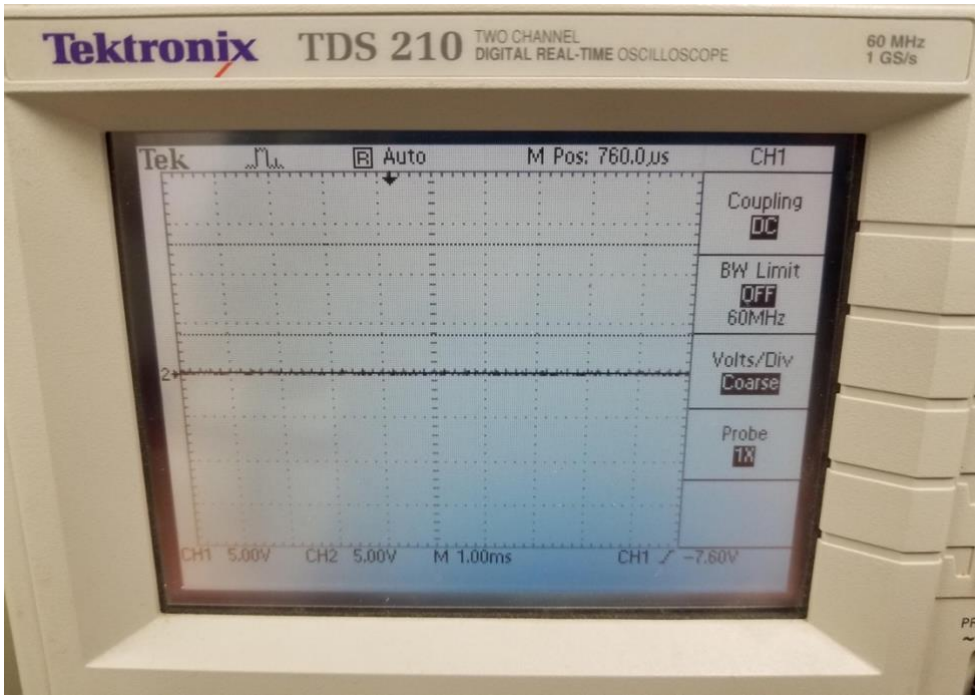

Figure 6.13: Oscilloscope Measuring Zero Volts

6.3.3 Adjustment of the Signal Zero

To adjust the signal zero, connect the BNC output (rear face) of the unit onto an oscilloscope. Submerge the tips of the probe in water to produce a signal output that should be at 0 volts as seen in Figure 6.13. Turn the coarse potentiometer clockwise in order to go from a negative to zero. Then turn the coarse potentiometer anticlockwise to go from a positive voltage to zero. Using the fine potentiometer, sharpen the adjustment.

6.3.4 Adjustment of the Gain of the Amplifier

The gain of the amplifier consists of adjusting the air signal value at 5 volts as seen in Figure 6.14. Take the probe out of the liquid, turn the gain potentiometer clockwise in order to increase the gain. Then turn the gain potentiometer anticlockwise to decrease the gain. If it is not possible to achieve an increase or a decrease in the gain using this method, then manually lift the

gain switch in order to increase the gain, and to manually lower the gain switch to decrease the gain.

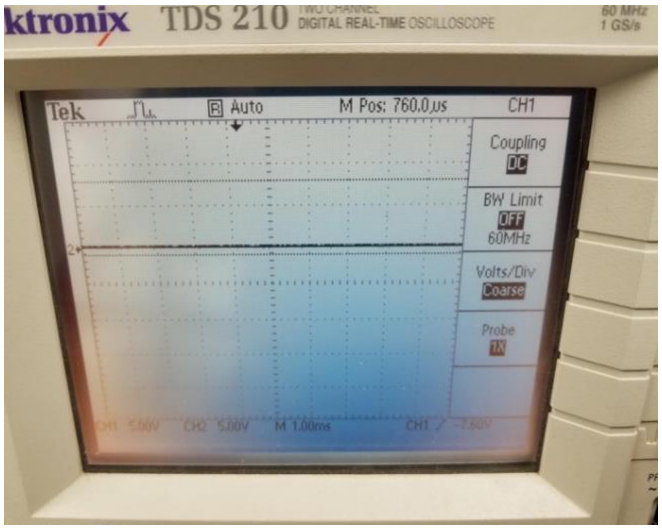

Figure 6.14: Oscilloscope Measuring Five Volts

6.3.5 Fine Adjustment of the Signal

Submerge the probe successively in the water and in the air. Then check the signal modulation from 0 volts in water to 5 volts in the air. Using a slightly higher voltage than 5 volts is recommended to avoid problems linked to the slight damage over time due to normal use, or dirt on the sapphire dips.

6.4 Two-Phase Probe Validation

Before taking two-phase measurements, the probes measurement technique must be validated to ensure the probes are calculating the correct void fraction and velocity measurements. Using the set-up in Figure 6.15, the acrylic box was partially filled with water to submerge the probe in water to simulate an environment where the sapphire tips are not

subjected to air. After that, air is injected directly into the probes so that the bubbles come into contact with both sapphire tips to ensure the bubbles are detected by both sapphire tips for accurate void fraction and velocity measurements. To validate the measurement, the probe calculates a high-speed camera that captures the movement of the bubble at 5000 fps, which was also used to calculate the velocity of the bubbles. By using the distance between the sapphire tips and the frames captured with the high-speed camera, the velocity of the bubble can be calculated and compared with the results in the ISO software.

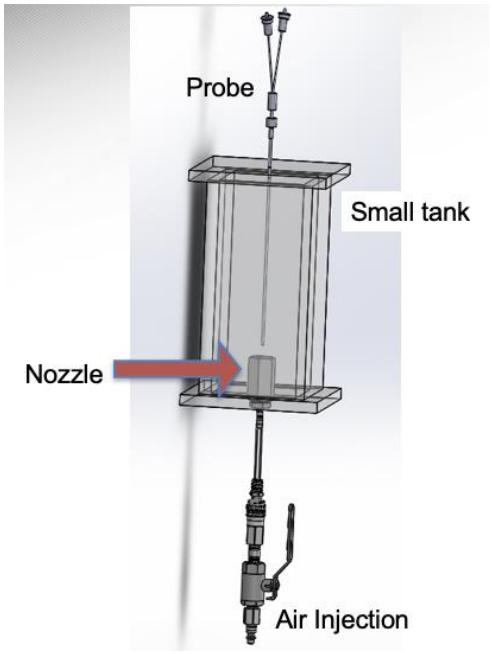

Figure 6.15: Experimental Velocity Validation Set-Up

After conducting the experiment and using the high-speed camera to film the speed of the bubble, the following calculation was performed using the distance between the sapphire tips or the e parameter of the probe.

$$Velocity = \frac{distance}{time} = \frac{0.00065\ m}{0.004\ s} = 0.1625\ \frac{m}{s} \qquad \text{(Eq. 1)}$$

When comparing the calculated velocity using equation 1, to the velocity produced by the ISO software, the velocity is the same. In addition, in Figure 6.16 the cross-correlation peak value is above 0.7 which means the result is statistically converged. Also, in Figure 6.16 the ISO velocity can be seen. This test proves the ISO is calculating the velocity correctly using the cross-correlation that relates to the distance between the sapphire tips.

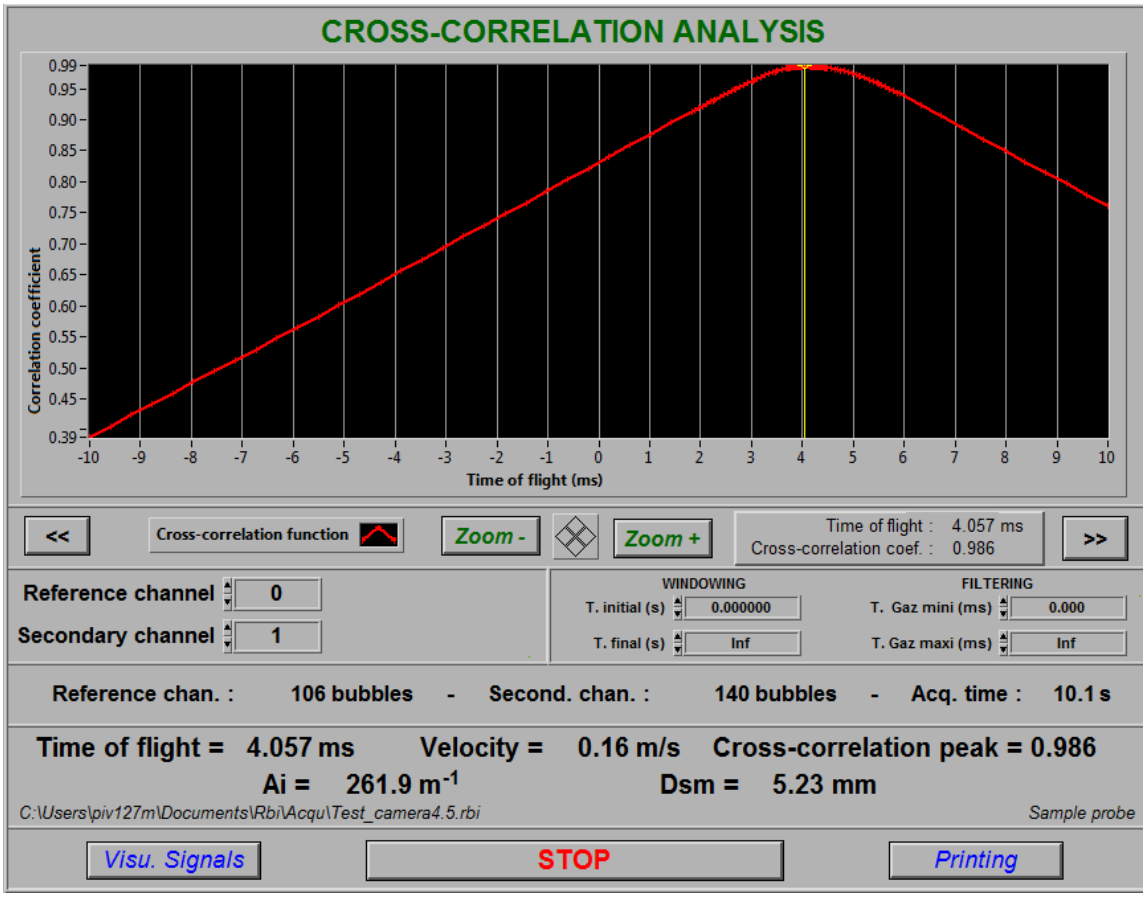

Figure 6.16: Velocity Validation ISO Calculated Velocity

6.5 Additional Experiment

6.5.1 Test Description

After putting the optical sensor probes in the RCCS and taking measurements, the probes still had a cross-correlation peak value that was under 0.7. The tank used in the bubbly flow part of the experiment allowed for air to be injected into a nozzle which was attached to an air diffuser as seen in Figure 6.17. This air diffuser allowed for a bubbly flow (Figure 6.18) to be simulated while taking away all parameters that were uncontrollable in the RCCS. Moreover, the bubbly flow in the tank could be simulated for a longer time duration than in the RCCS.

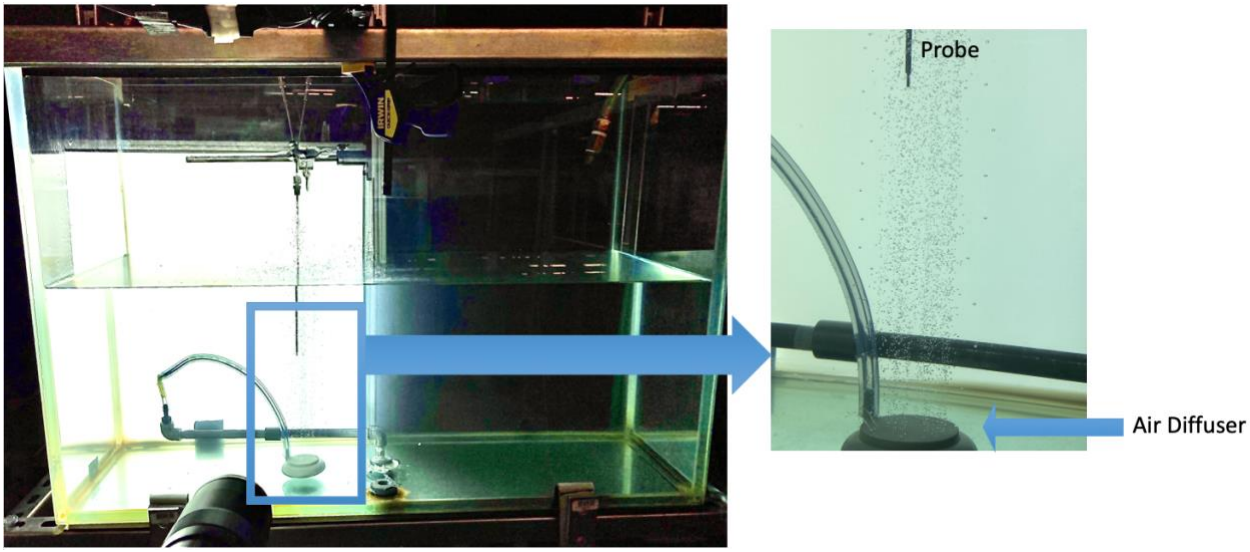

Figure 6. 17: Tank Cross-Correlation Experiment Setup

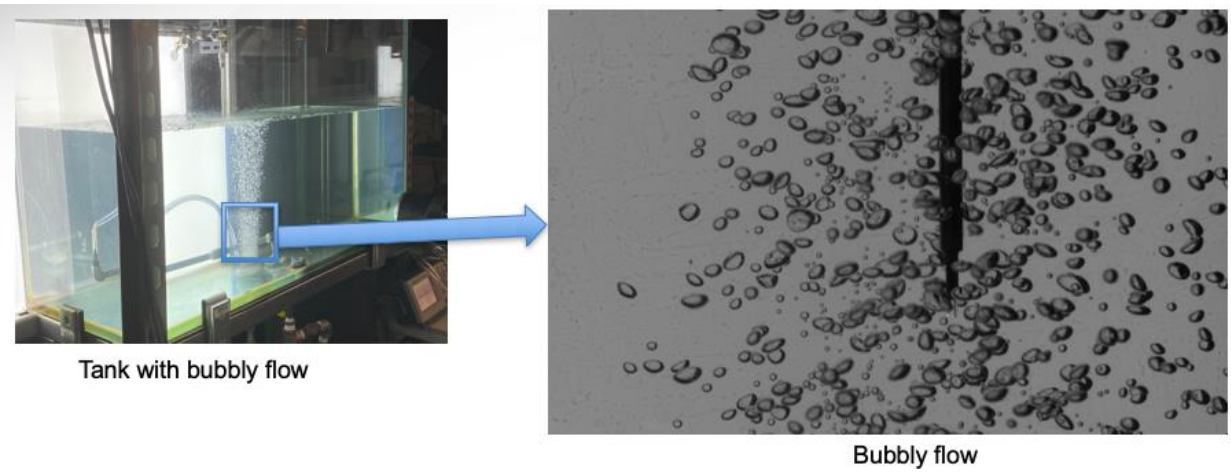

Figure 6.18: Tank Cross-Correlation Experiment Bubbly Flow

6.5.2 Bubbly Flow Experiment

After taking a measurement for an hour duration, the bubble number can be seen in Figure 6.19. The bubble number is the number of bubbles the probe counted during the acquisition time. In Figure 6.20, the cross-correlation peak can be seen to be 0.473, which is too low for a valid result.

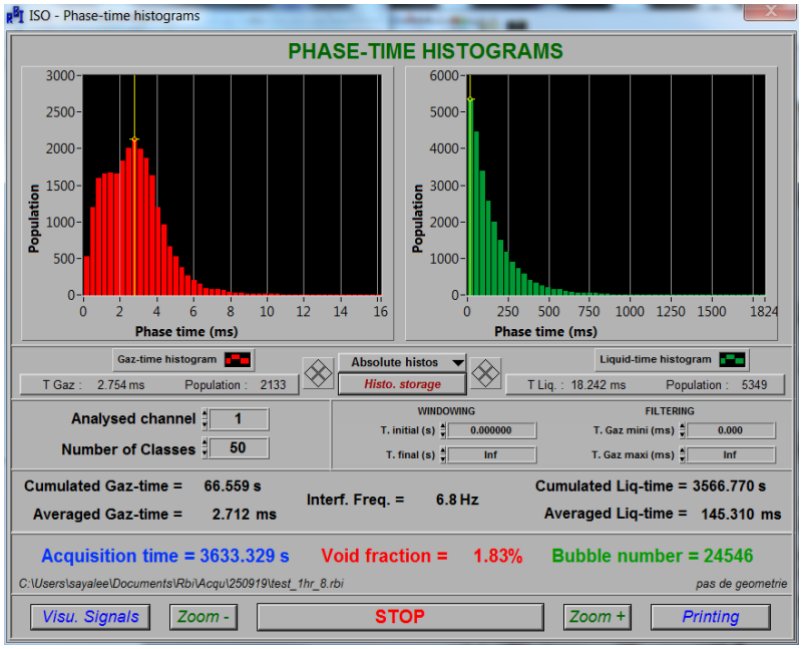

Figure 6.19: Void Fraction Result Test 1 for 1-Hour Time Duration

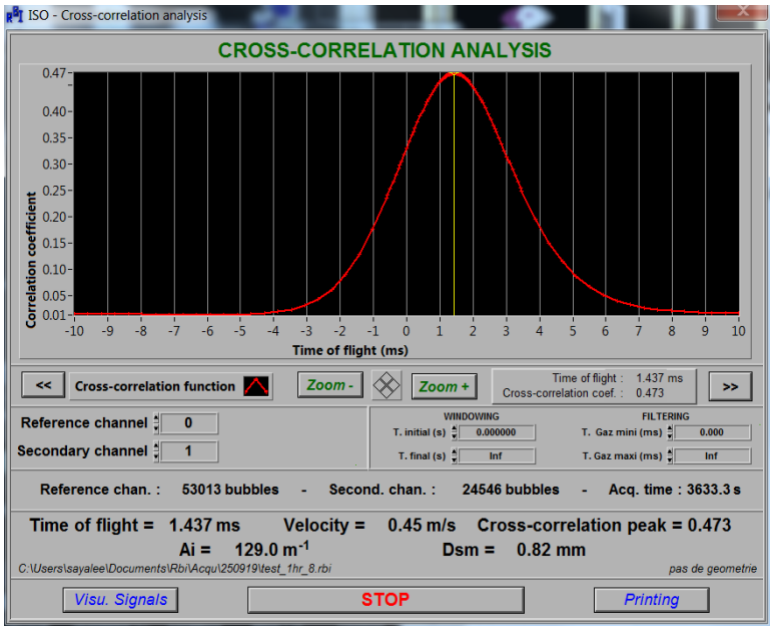

Figure 6.20: Cross-Correlation Analysis for Test 1 in Bubbly Flow for 1-Hour Time Duration

Another test was conducted for an hour duration; the bubble number can be seen in Figure 6.21. Figure 6.22 shows the cross-correlation peak at 0.469, which is too low for a valid result. Due to the bubbly flow, a longer acquisition time would be needed to increase the value of the cross-correlation peak.

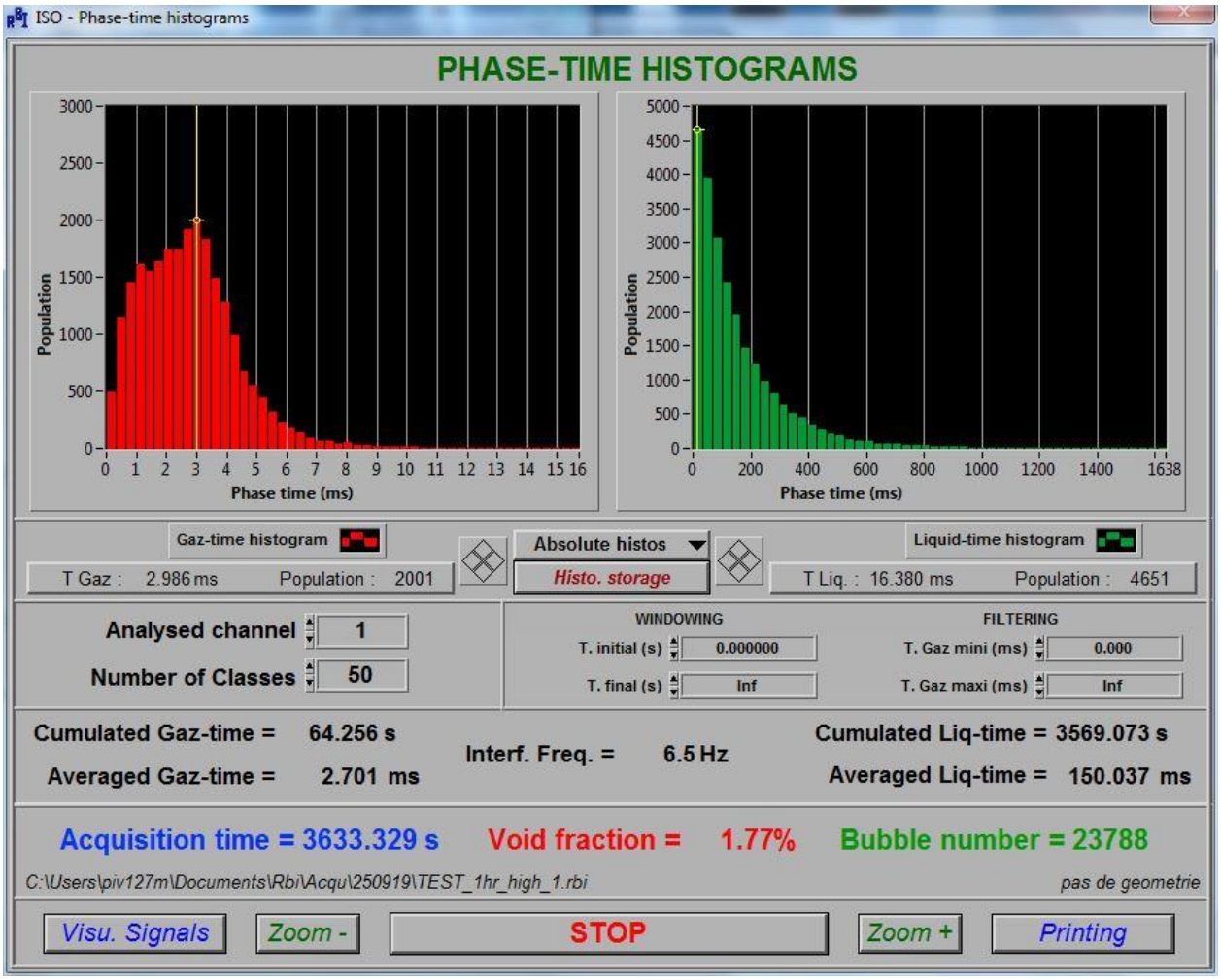

Figure 6.21: Void Fraction Result Test 2 for 1-Hour Time Duration

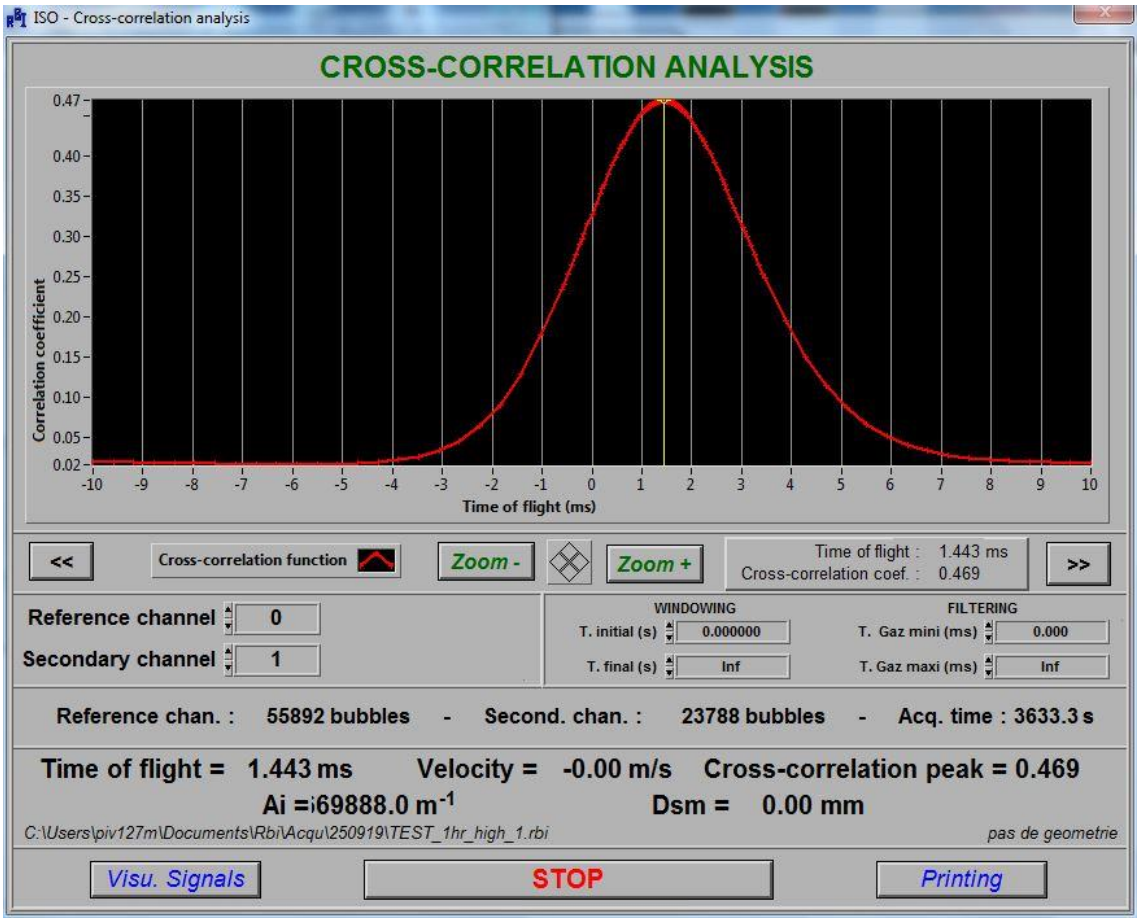

Figure 6.22: Cross-Correlation Analysis for Test 2 in Bubbly Flow for 1-Hour Time Duration

6.5.3 Large Direct Injection Bubble Experiment

Using the same tank, another experiment was conducted in which the bubbles were made larger by increasing the flowrate of air, and were directly injected into the sapphire tips. In Figure 6.24, the bubble number can be seen to be lower than when bubbly flow was simulated. This decrease in bubble number is due to the acquisition time being 1-minute, rather than 1-hour. Even though the acquisition time was reduced and the bubble size was increased, the cross-correlation peak value was 0.773. This cross-correlation peak value can be seen in Figure 6.25, which is an acceptable value for a valid result.

Figure 6.23: Large Direct Injection Bubble

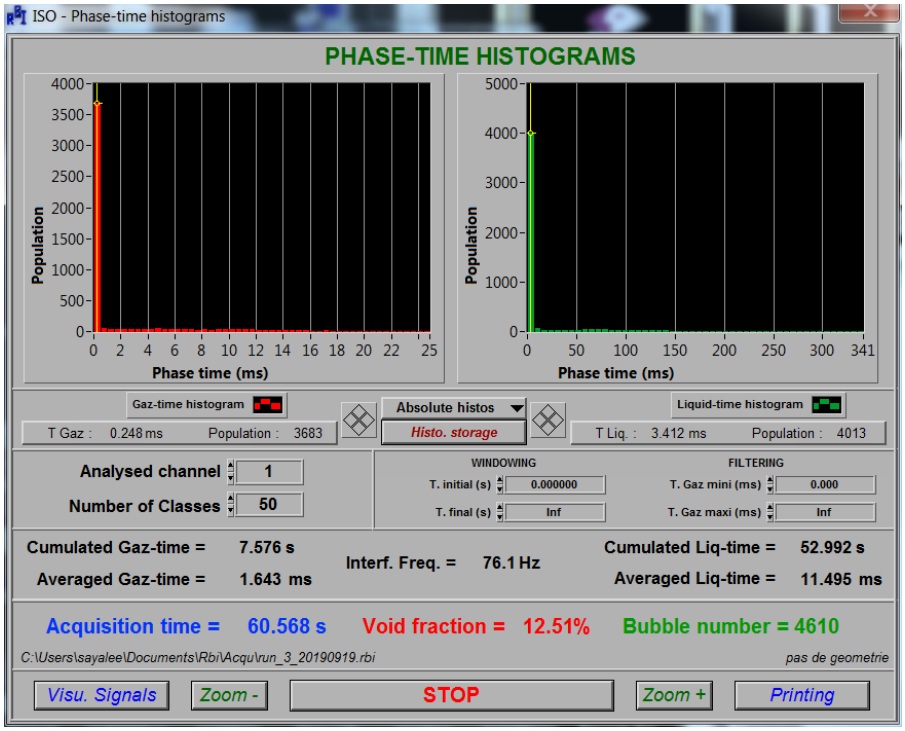

Figure 6.24: Cross-Correlation Analysis for Test 1 in Bubbly Flow for 1-Hour Time Duration

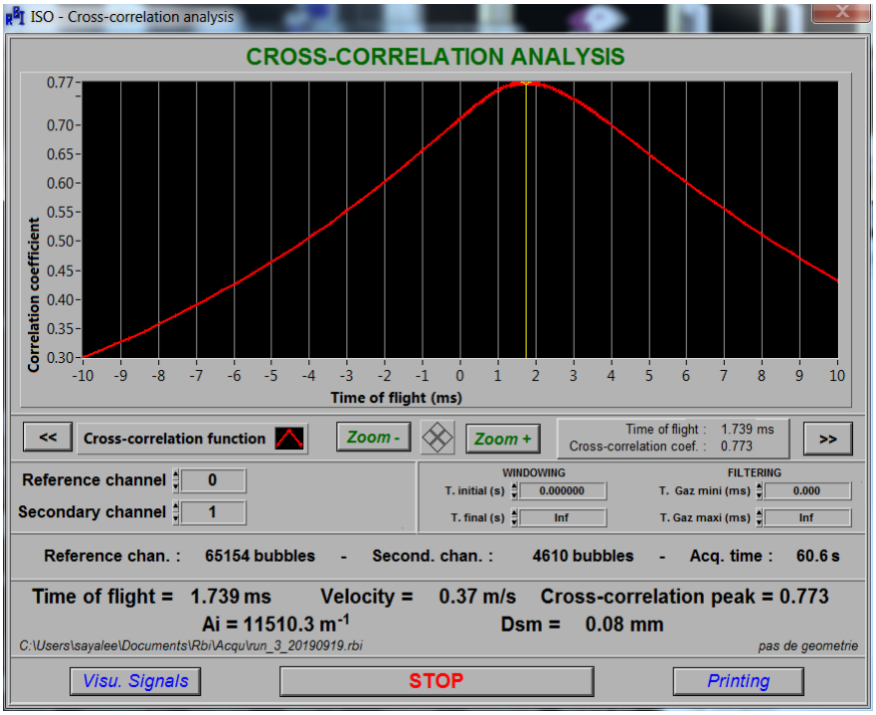

Figure 6.25: Cross-Correlation Analysis for Test 1 in Bubbly Flow for 1-Hour Time Duration

In Table 6.1 it can be seen that the cross-correlation peak was not at an acceptable value of 0.7 after an hour duration. This means to get the cross-correlation peak to be an acceptable value, the bubbly flow measurement with the optical sensor probes would have to be maintained for over an hour. In addition, increasing the bubble size or increasing the measurement time duration will cause the cross-correlation peak to increase.

Table 6.1: Cross-Correlation Peak and Acquisition Time for Corresponding Experiment in Tank

Experiment	Acquisition Time (s)	Cross-Correlation Peak
Bubbly Flow Experiment 1	3633	0.473
Bubbly Flow Experiment 2	3633	0.469
Large Direct Injection Bubble	60	0.773

6.6 Working Principle of the Opto-Electrical Unit

The opto-electrical unit receives a photon signal from the optical sensor probes. After receiving the signal, the opto-electrical unit shapes the signal and converts the signal to a TTL signal so that the signal can be sent to the ISO software. By using the automatic thresholding method of operation, the signal is transformed to a TTL signal. Figure 6.26 illustrates how the signal is shaped as well as how the upper and lower limits of the signal are defined. This upper threshold and lower threshold are defined when applying the calibration.

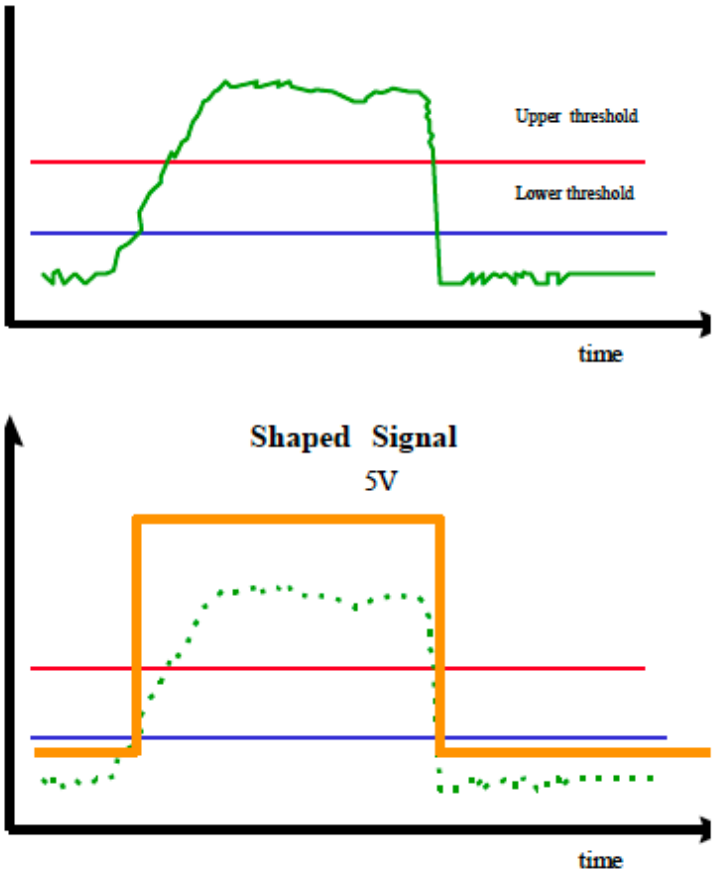

Figure 6.26: Signal Shaping (RBI, 2005)

6.7 Working Principle of the Acquisition Module

Inter-correlation analysis is based on the hypothesis that if all interfaces interfere with both probes without creating any disturbance, the phase indicating functions are identical, except with a time shift. The shift is defined by the gas time common to both PIFs in Figure 6.27, which can be viewed in the ISO software. It was further illustrated the initial gas time that was common to both PIFs contained a small distance, but over time, the distance increased. However, the acquisition module was able to stabilize the signal received by the opto-electrical unit. Later, the acquisition module was able to return the shift value to the initial state.

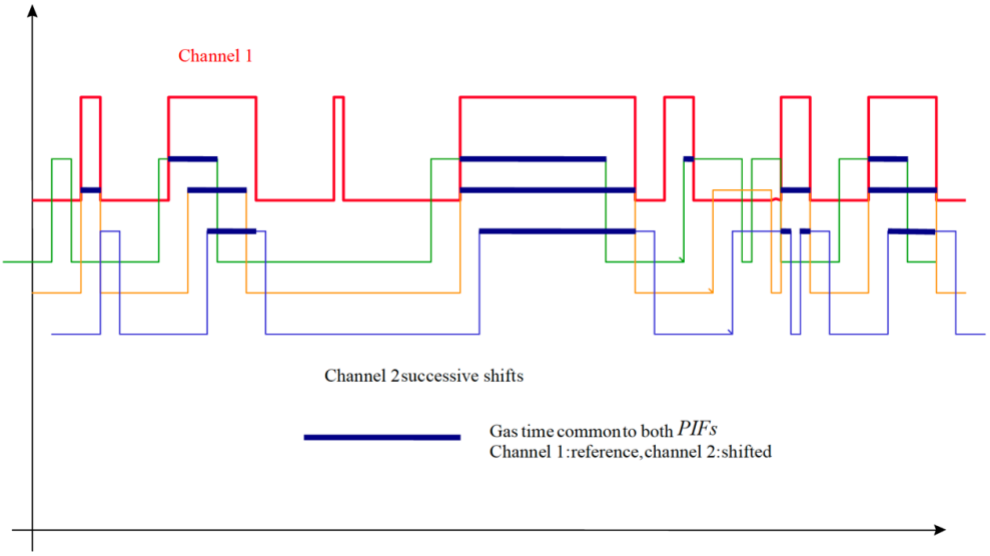

Figure 6.27: Intercorrelation Principle Signal (RBI, 2005)

Figure 6.28 represents the shift value as initially small after the calibration. However, as the time duration increased the shift value increased as well. Yet when the shift value was at a maximum, the acquisition module regulated the signal to the initial value. Furthermore, this method may be implemented despite the distance between the probes.

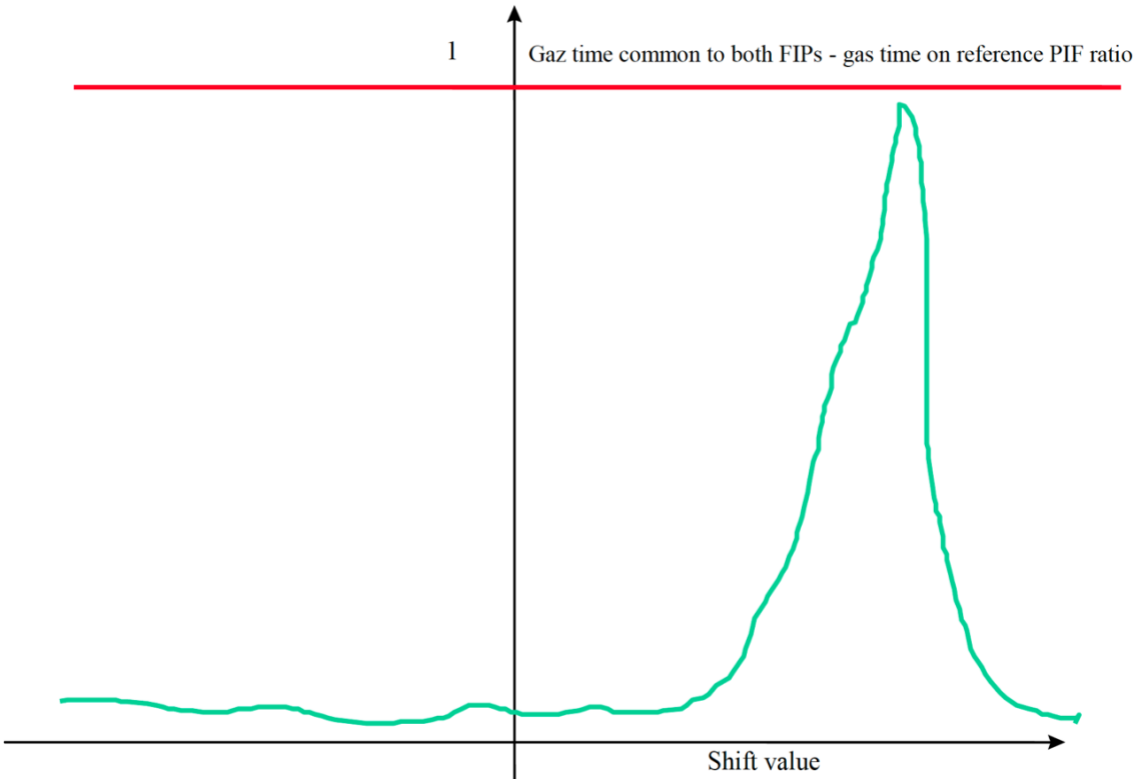

Figure 6.28: Intercorrelation Principle Shift Value (RBI, 2005)

6.8 Application of the Oscilloscope Unit

Once the Signal is received it can be viewed on an oscilloscope and is used with calibrating the system. Likewise, the signal can be measured on the oscilloscope to determine the output voltage from the opto-electrical unit. Figure 6.29 shows how a typical signal would look, while in figure 6.30 shows the same signal in the ISO software.

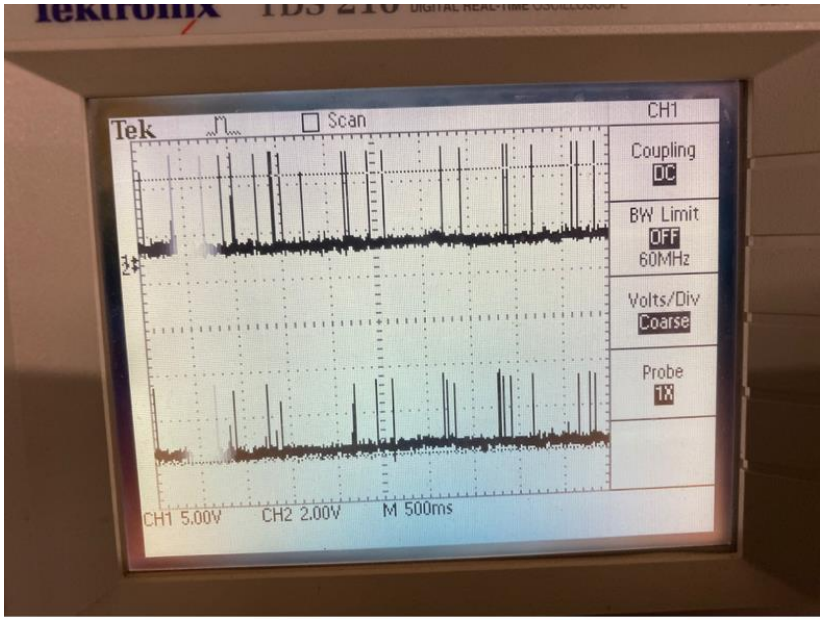

Figure 6.29: Signal Viewed on the Oscilloscope

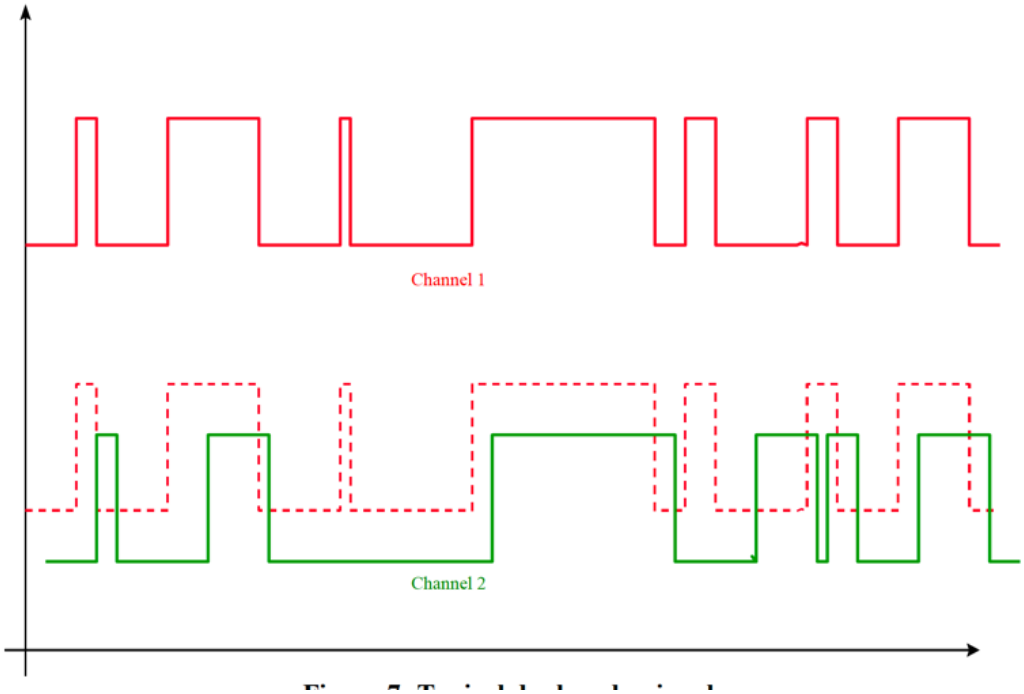

Figure 6.30 Signal From the Probe Received in the ISO Software

6.9 ISO Software

After the signal is received by the opto-electrical unit and is converted to a TTL signal, the acquisition module stabilizes the signal and sends it to the ISO software for further analysis. Once received by the ISO software, the software makes two useful calculations for this study. In Figure 6.31, the void fraction calculated by the ISO software is displayed. This void fraction is calculated using equation 2. In addition, Figure 6.32 represents the velocity that is calculated by the ISO software. In this calculation, the ISO software uses a cross-correlation equation that correlates the distance between the sapphire tips, and the total acquisition time to calculate a velocity. The velocity is calculated using equation 3 by the ISO software where the e parameter or distance between tips is used as distance. For the analysis to be statistically valid, the cross-correlation peak provided by the software must be greater than or equal to 0.7.

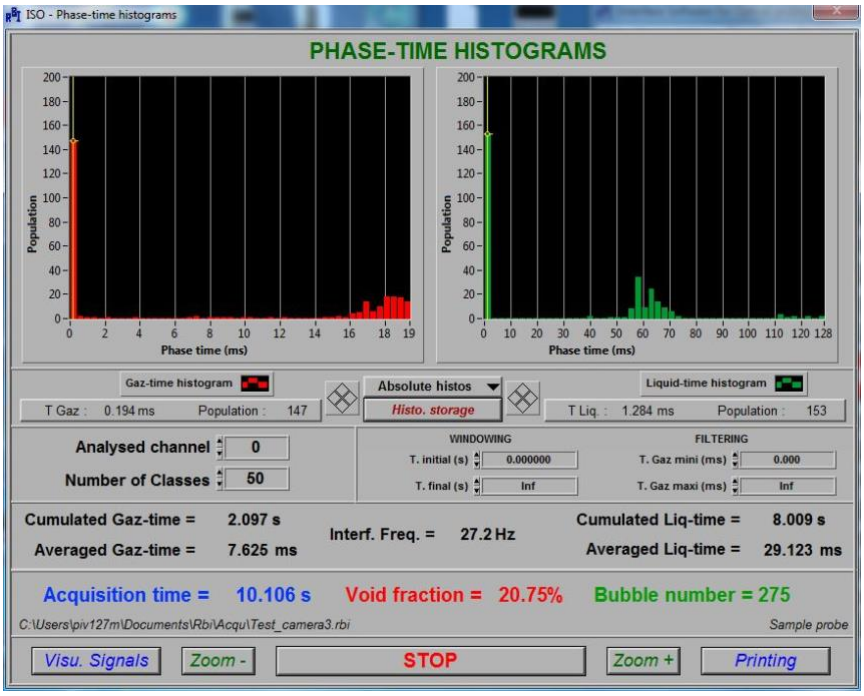

Figure 6.31: Void Fraction Histogram

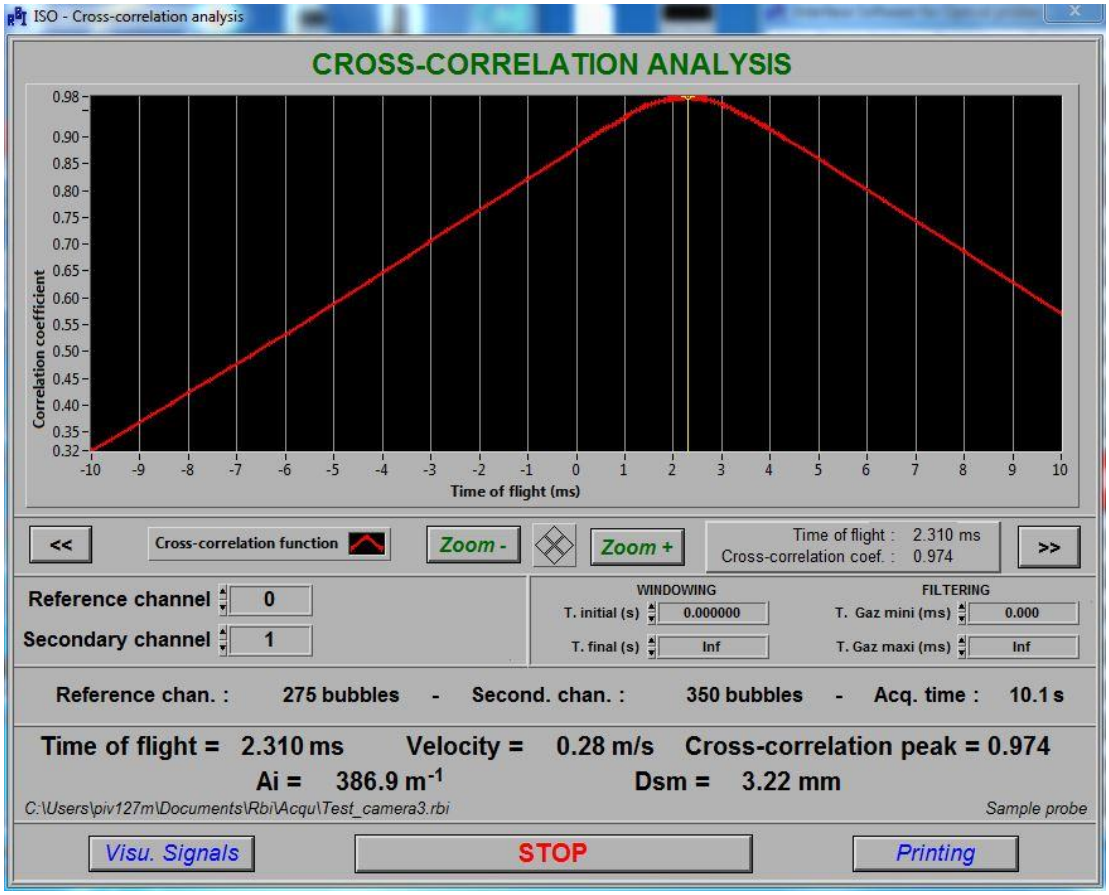

Figure 6.32: Velocity Cross-Correlation Analysis

$$Void\ Fraction = \frac{time\ gas\ is\ detected}{Total\ aquisition\ time} \qquad \text{(Eq. 2)}$$

$$\text{Average } Velocity = \frac{distance\ between\ tips}{Total\ aquisition\ time} \qquad \text{(Eq.3)}$$

7. EXPERIMENTAL RESULTS

7.1. Test Conditions and Preparations

The RCCS facility was filled using a pump to transport water from the inlet of the risers. The facility was filled to the water level at the top window of the tank. Once filled, an air bubble was released to ensure the abundance of air trapped in the tank did not affect measurements. To ensure flow stability, the facility was left overnight. The following day, the data acquisition unit was started as well as the LabVIEW VI. Next, the three 8 kW heaters were turned on and set to 38% of the total power. Using the same camera set up as previously described, the cameras were powered on, and the pulse generator for the synchronization of the cameras was turned on as well.

7.2. Test Description

In this experiment a test is conducted in the RCCS in which the two-phase phenomena will be observed using three phantom miro cameras. Each of the cameras has a 50 mm lens and the camera speed is set to 240 fps. A light panel is place behind the transparent glass upper manifold to have light exposure to the camera for clear visible bubbles to be recorded by the cameras. The cameras were placed in front of the upper manifold in order to view three risers per camera. In addition to observing the two-phase phenomena, temperature of the water was measured at different locations in all 9 risers as well as the inlet and outlet of the riser panel. These temperature measurements were evaluated to correlate void fraction to the temperature. The expected outcome is that under bubbly flow conditions the flow will be symmetric due to an even distribution of the flowrate in each riser. Due to the cross-correlation peak not reaching a

value of 0.7 during bubbly flow, high-speed cameras, thermocouples, and a magnetic flowmeter were the main measurement devices in this experiment. Using the high-speed cameras, the recording time duration is 34 seconds. This will allow for the cameras to record a single bulk boiling cycle. The phase progression is non-condensable gas, vapor formation, bulk boiling, and reverse flow.

7.3. Flowrate of the RCCS during Transient Scenarios

In Table 7.1 the movie times are available to see the points of interest that were captured by the high-speed camera. In Figure 7.1, the flowrate is shown with the corresponding movie set times that all three high-speed cameras captured. In all graphs the start times are displayed for each movie set recorded by all three cameras in the Table 4. Moreover, all graphs start from 0 or the initial point of recording which coincides to the movie set times displayed in Table 4.

Table 7.1: Two-Phase Observation Movie Times

Movie Set	Times (s)
1	0
2	1454
3	1662
4	1945
5	5782
6	6160
7	6371
8	6659
9	6875
10	7118

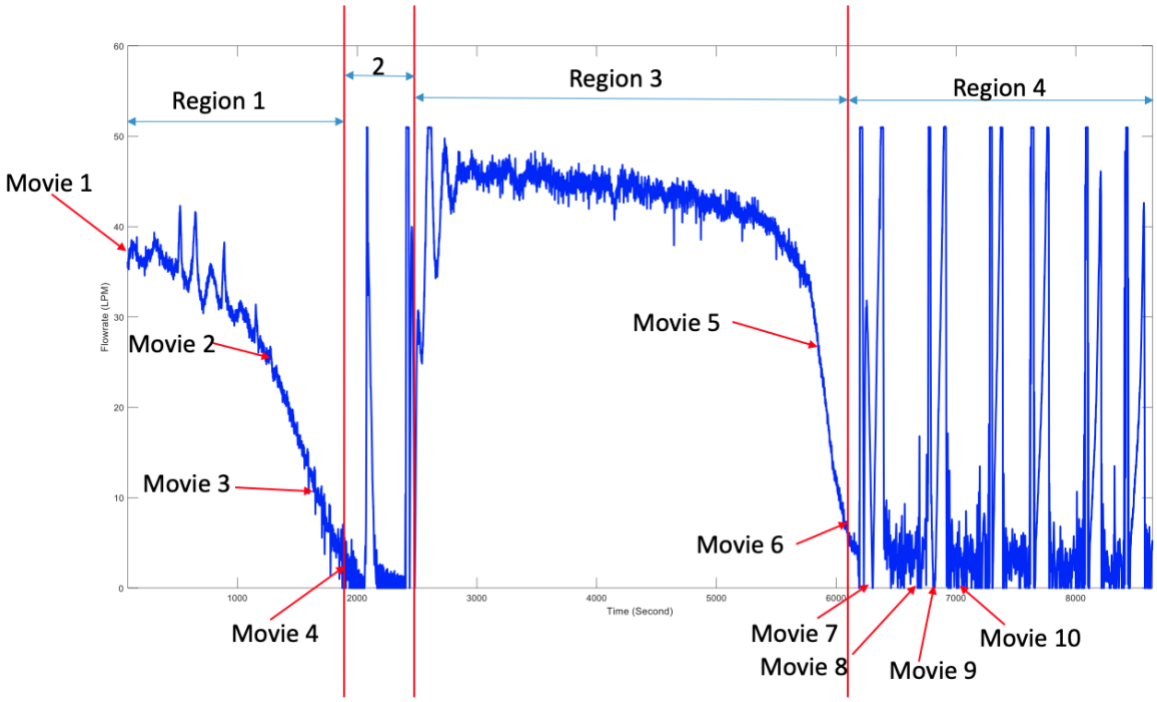

Figure 7.1: Flowrate of the Water in the RCCS and Corresponding Movie Times

Looking at Figure 7.2 in region 1, the riser panel is heated by three 8 kW electric heaters operating at 38% of the total power until air bubbles are released. These air bubbles are entrapped in the pipe walls in the riser after filling the RCCS facility. After air bubbles are formed, the flowrate drops down to 0 L/min. In region 2, the flowrate reaches zero, and the water in the riser panel begins to boil. Next, in region 3 the vapor bubbles have been quenched, and the facility water temperature decreases, causing the flowrate to increase. This heating that occurs in region 3 has a long duration time due to heat losses experienced in the system. While in this region, the flowrate begins to decrease causing an increase in temperature. In Table 7.2, the times of the air bubble release, vapor formation, bulk boiling, and reverse flow are illustrated. In addition, the corresponding movie set is displayed in Table 5.

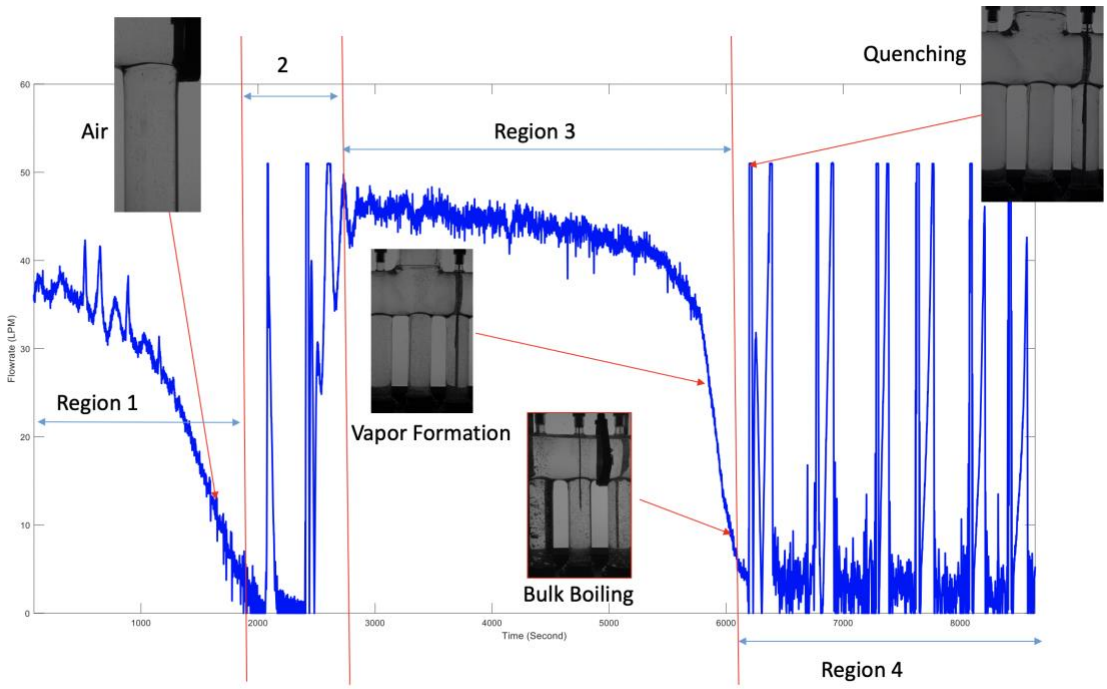

Figure 7.2: Flowrate at the Inlet of the Riser Panel

Table 7.2: Bubble Times from RCCS Using Cameras

	Movie Set	Time (s)
Air	3	1662
Vapor Formation	5	5782
Bulk Boiling	6	6160
Reverse	6	6166

Figure 7.3 displays all 9 risers with corresponding flowrate of water. In this graph it can be seen that as the temperature increases, the flowrate decreases. This can be viewed especially in region 4 when the heating cycles occurs. Furthermore, in Figure 7.4 is a zoomed image of region 4 that allows for a more detailed visualization of the temperatures during each boiling

cycle. In this figure, it is further illustrated the flowrate of the water is decreased when the temperature approaches boiling, and flowrate is increased as temperatures decrease. At 6,198 seconds in Figure 7.4, the flowrate increases as temperature decreases. Once the flowrate is zero, the boiling phenomena starts to occur until the flowrate increases. As the flowrate increases, it causing a decrease in temperature. This succession of boiling and temperature decrease continues to occur for the remainder of region 4.

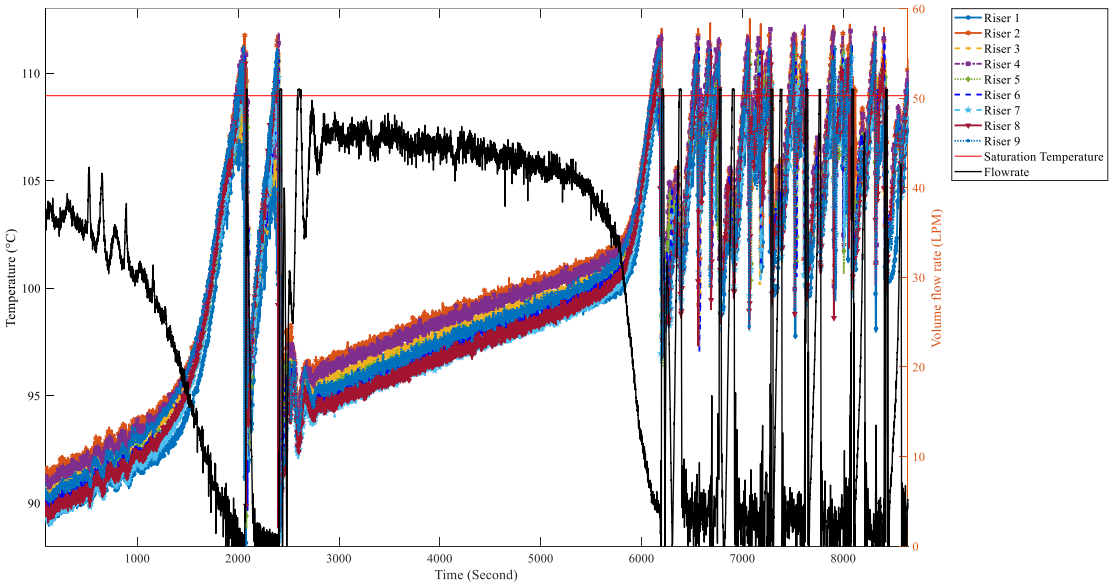

Figure 7.3: Temperature of all 9 Risers at Position 5 with Corresponding Flowrate.

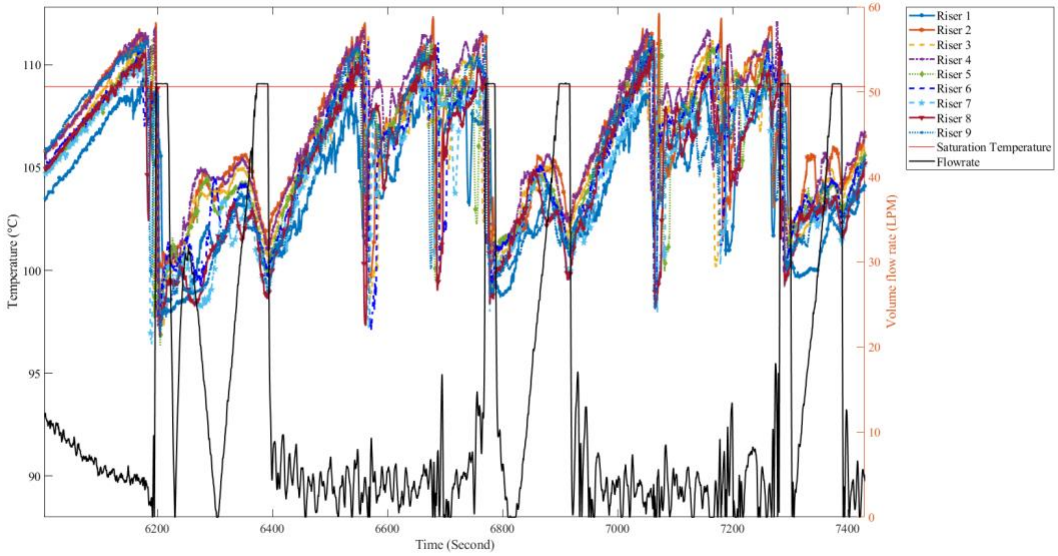

Figure 7.4: Zoomed Temperature of Boiling Cycle

7.4. Air Bubble Release

As the water in the riser heats up, Figure 7.5 shows the air bubbles that appear in riser 7 once the flowrate starts decreasing, while temperature increases. In Figure 7.6, the water temperature can be viewed from all the risers as non-condensable gas bubbles are released. The lowest temperature is from riser 4 at 88 degrees Celsius, while the highest temperature is from riser 2 at 91 degrees Celsius. This is lower than the saturation temperature of the water which was calculated to be 108.95 degrees Celsius. At this water temperature, there is no vapor formation, and the flowrate is about 41 L/min.

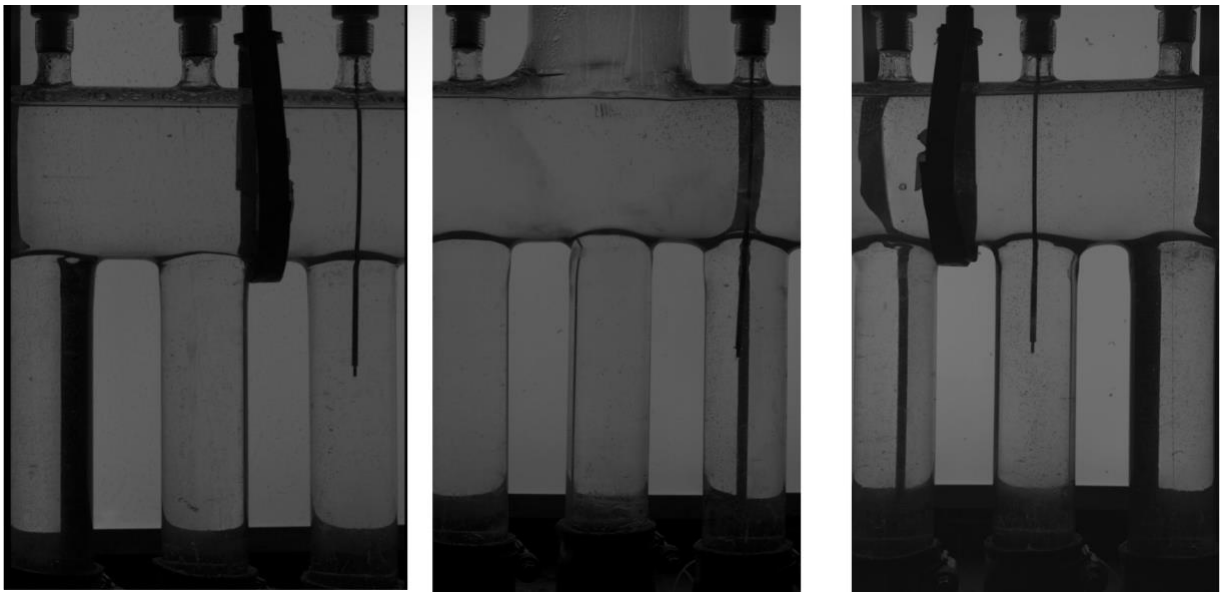

Figure 7.5: Non-Condensable Air Bubbles

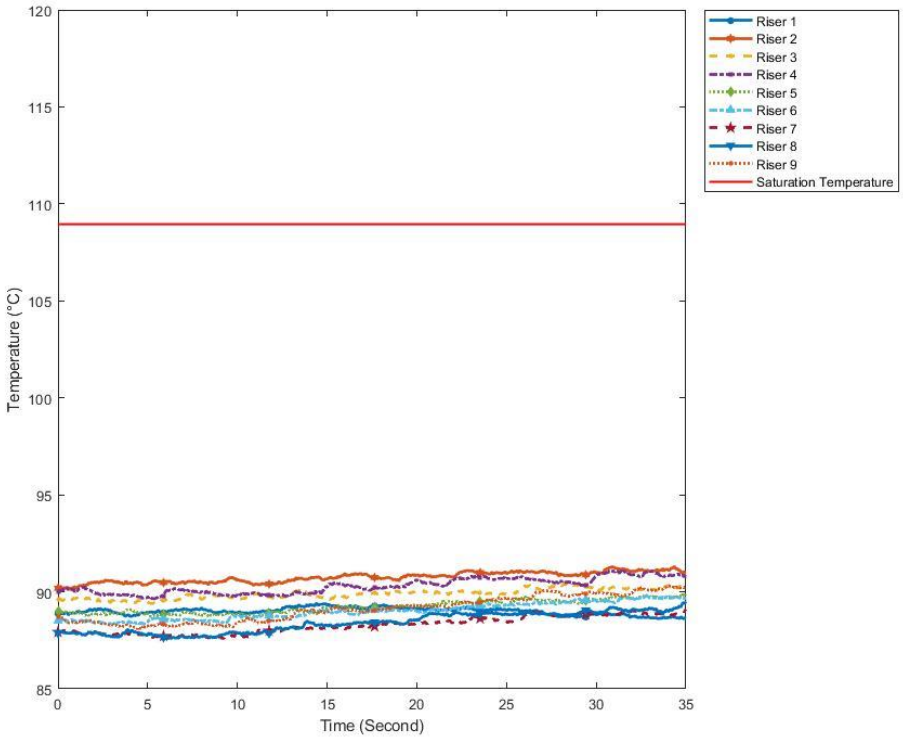

Figure 7.6: Non-Condensable Gas Bubble Temperatures From all Risers

7.5. Vapor Formation

As the water in the riser heats up further, Figure 7.7 illustrates the vapor formation is symmetric in all the risers. Additionally, the flowrate of the water in the riser panel simultaneously continues to decrease. Yet, as the flowrate decreases, the temperature also increases. In Figure 11.8, the vapor bubble temperatures can be seen from all of the risers.

The lowest temperature is from riser 1 at 105 degrees Celsius, while the highest temperature is from riser 9 at 109 degrees Celsius. In this phase progression only riser 9 is above saturation temperature calculated at 108.89 degrees Celsius. This result is right in line with the observation taken with the high-speed camera. In this stage bubble size of the vapor is uniform and there is no bubble deformation occurring. At this temperature there are no air bubbles.

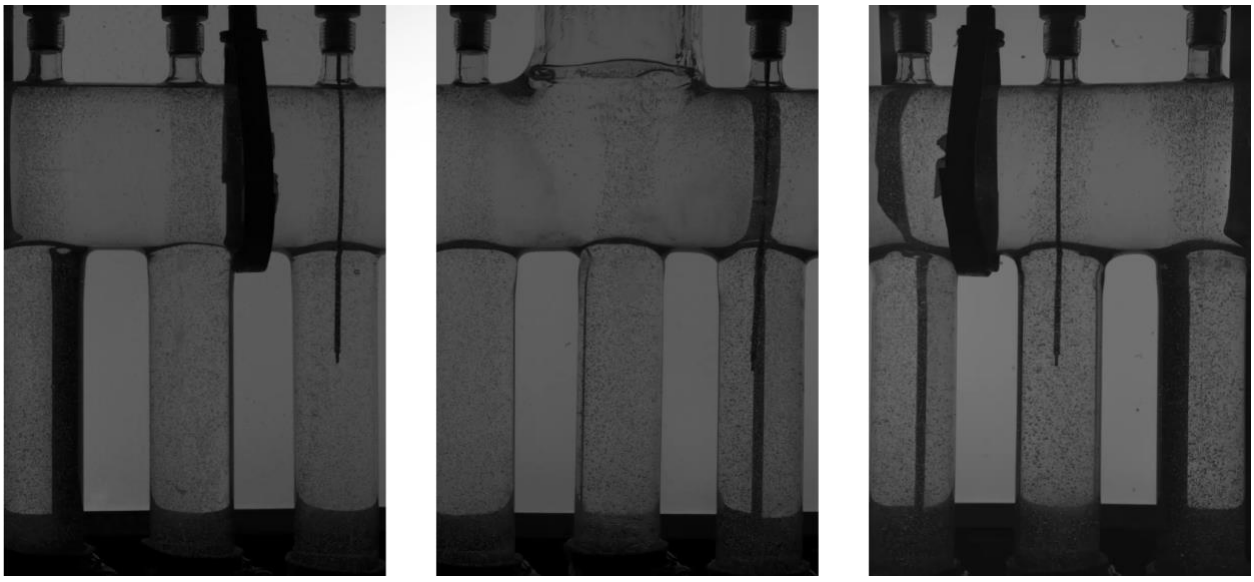

Figure 7.7: Vapor Formation

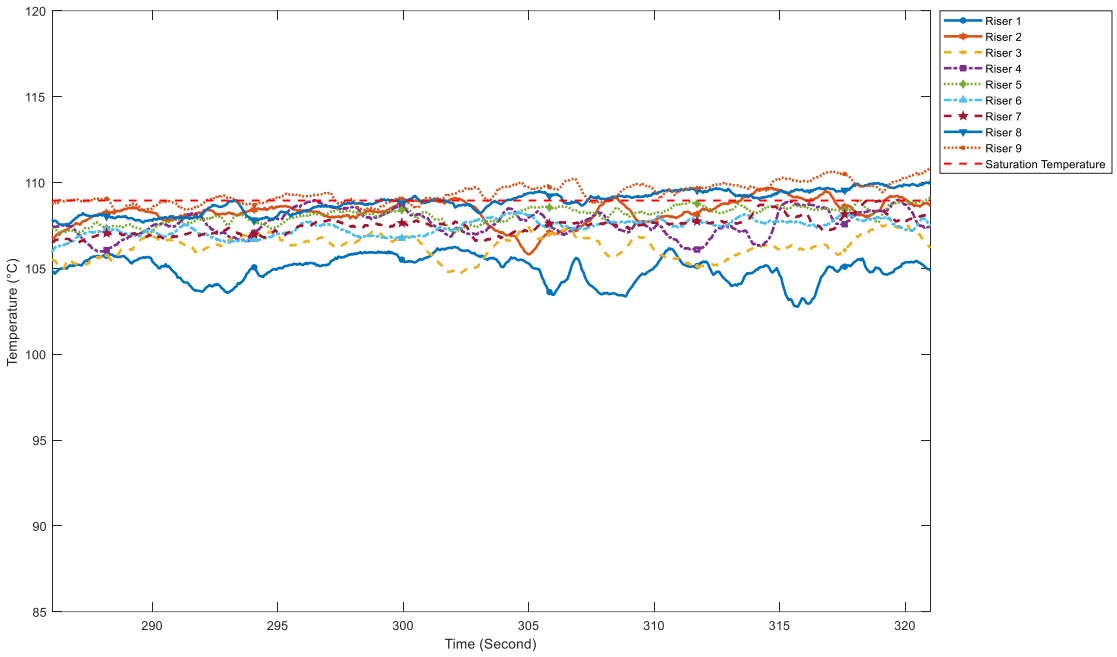

Figure 7.8: Vapor Formation Temperatures of all Risers

7.6. Bulk Boiling Phenomena

Next, using movie 5 as the water in the riser heats up further, Figure 7.9 shows the vapor density is not symmetric in any of the risers. At 4120 seconds in riser 6, the bubbles are larger and travel at a faster speed than any other riser. While at the same time, the flowrate of the water in the riser panel has decreased to 0 L/min. As the flowrate decreases, the temperature also increases. After the increase in bubble velocity occurs, then the temperature in riser starts to decrease as the flowrate of the water increases.

In Figure 7.10 the temperatures of the water when bulk boiling when occurs. The temperatures will go above saturation without complete vaporization because the mixture of gas and water is being measured. When in a phase transitioning state, the water will not exceed the saturation temperature until it is completely vaporized. However, the gas can achieve a superheated state which will cause a temperature higher than saturation temperature to be measured. Due to the mixture where the gas is superheated at a higher temperature than saturation and water at saturation, the temperature of the mixture is higher than the saturation of water. When the bulk boiling cycle begins, there is first a reduction in temperature in riser 6. When riser 6 is above saturation temperature, the bubble size is larger than the bubbles in the other risers. Some bubbles in riser 6 are deformed and not uniform. This large bubble size also travels at a faster bubble velocity than the bubble velocity for the vapor formation. After riser 6 decreases in temperature, 3 seconds later riser 8 decreases in temperature. This repetition of risers heating up and cooling down occurs for a 35 second duration. This allowed all of the risers stay below saturation temperature.

Figure 7.11 displays all risers, at 0 seconds. It can be seen the riser with the highest velocity is riser 6. Figure 7.12 displays all risers at 10 seconds. It can be seen that the riser with

the highest velocities are riser 7 and 9., Figure 7.13 displays all risers, at 20 seconds. It can be seen that the riser with the highest velocity is riser 5. Figure 7.14 displays all risers, at 30 seconds. It can be seen that the risers have reduced in temperature and the bubbles are quenched.

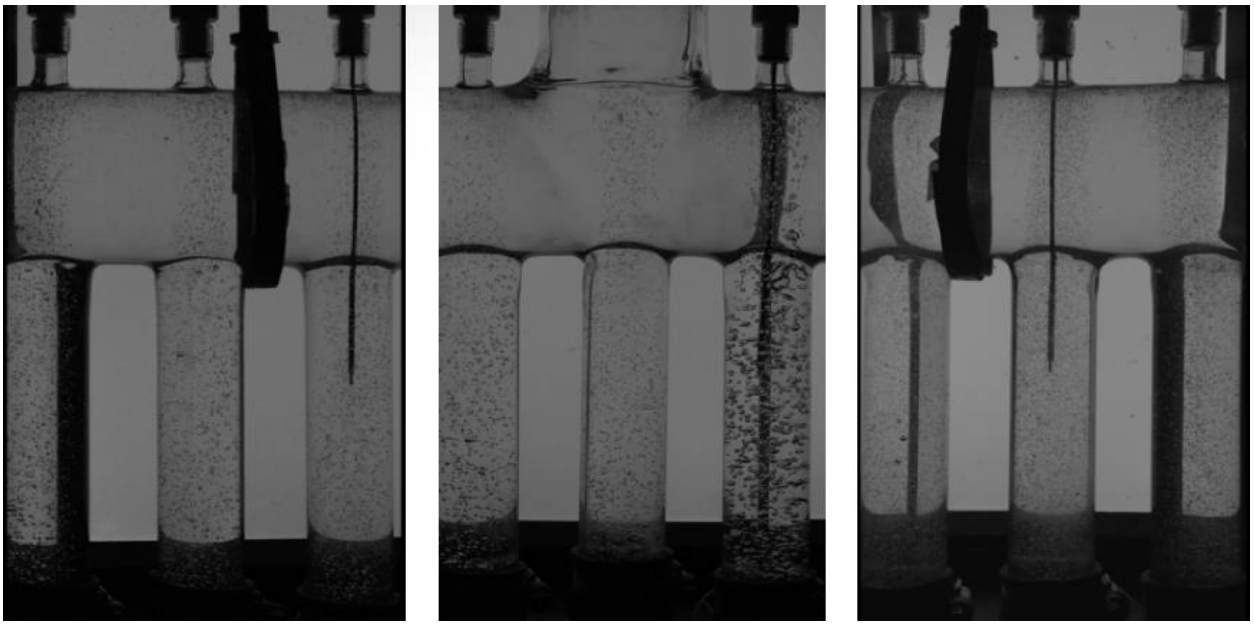

Figure 7.9: Boiling Phenomena

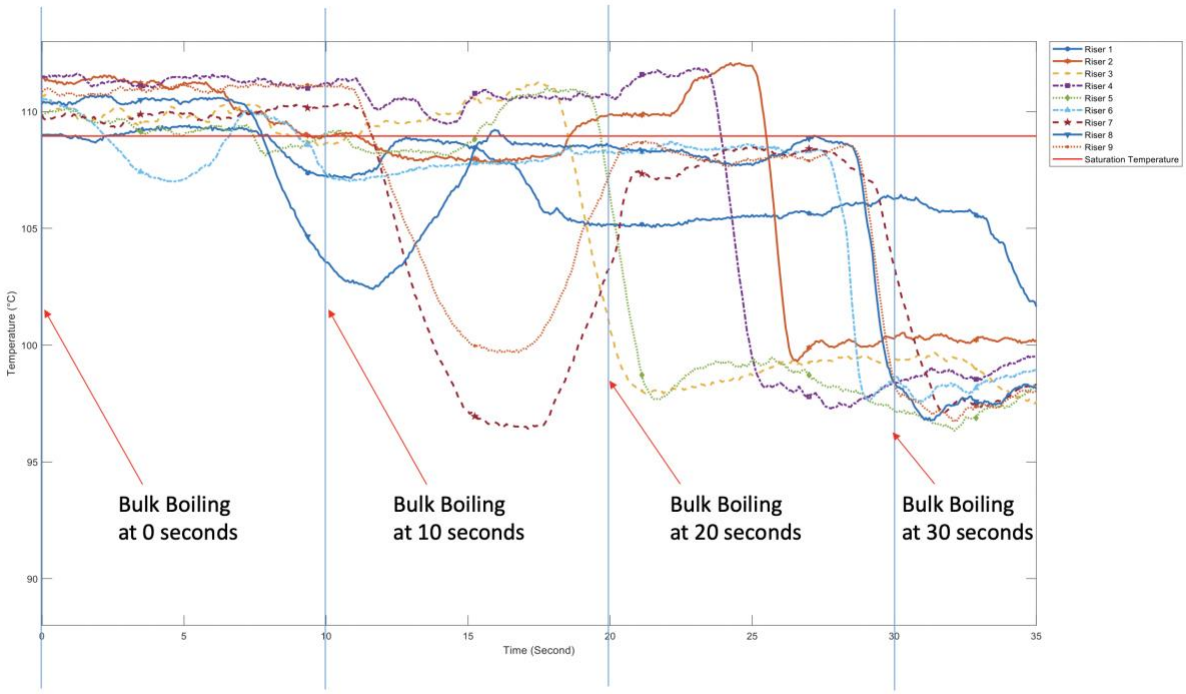

Figure 7.10: Boiling Temperatures of all Risers During Boiling Cycle

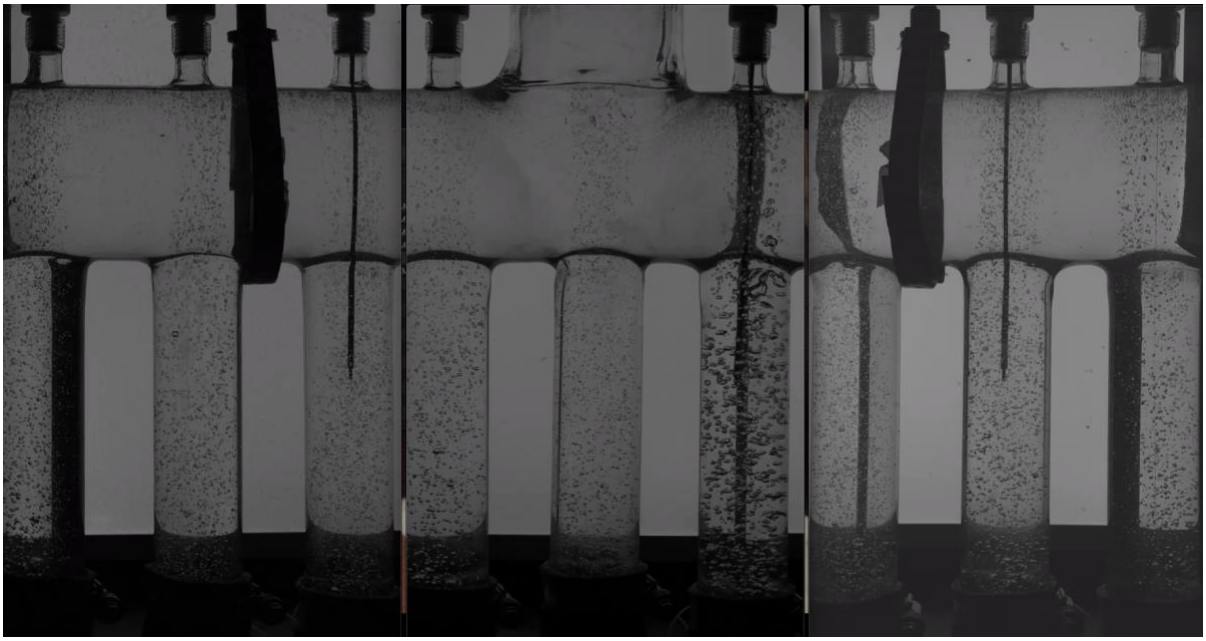

Figure 7.11: Boiling at Time 0

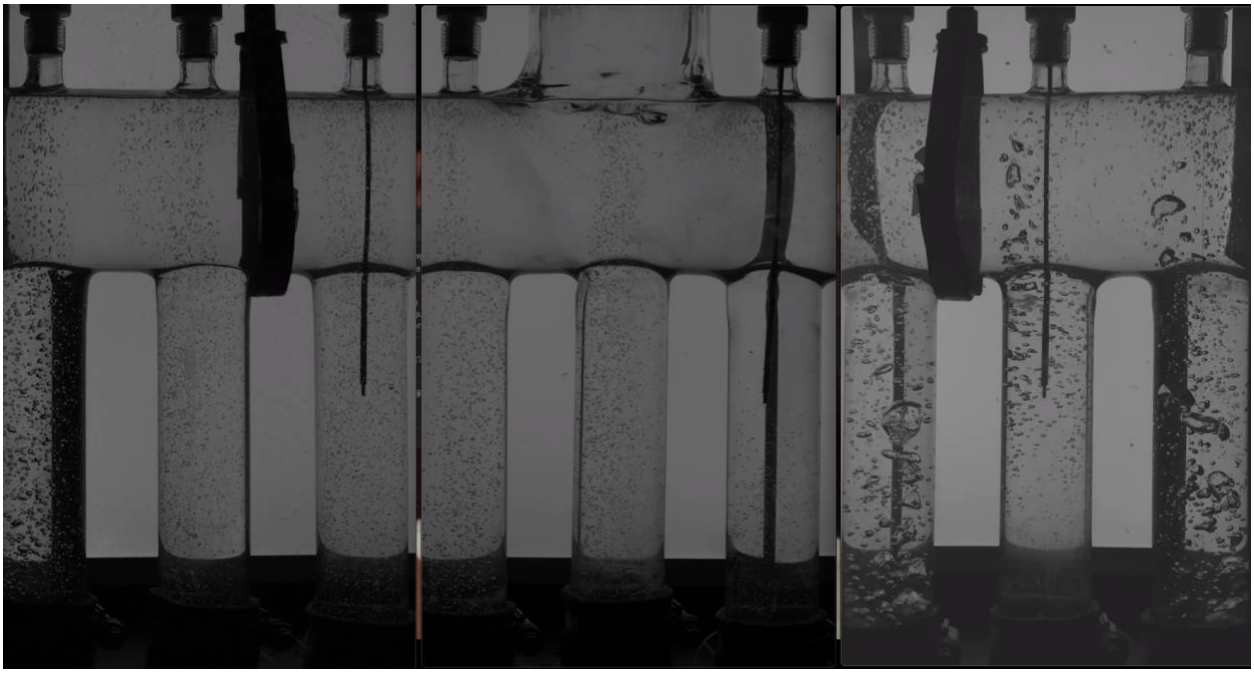

Figure 7.12: Boiling at Time 10

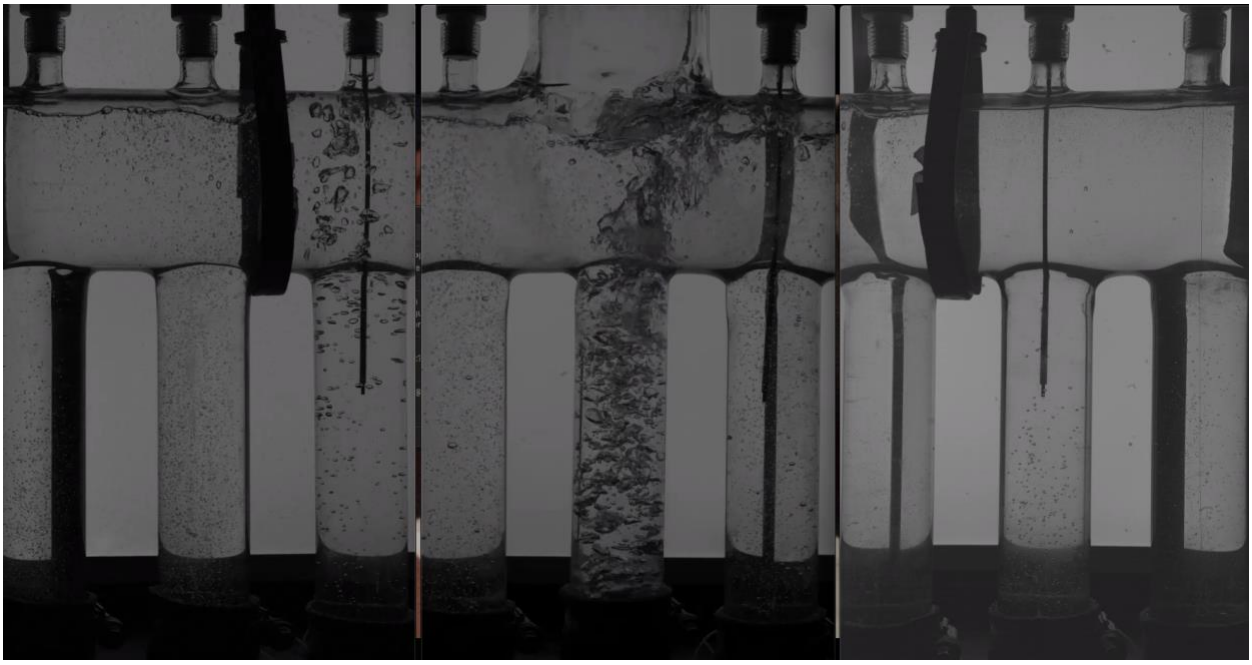

Figure 7.13: Boiling at Time 20

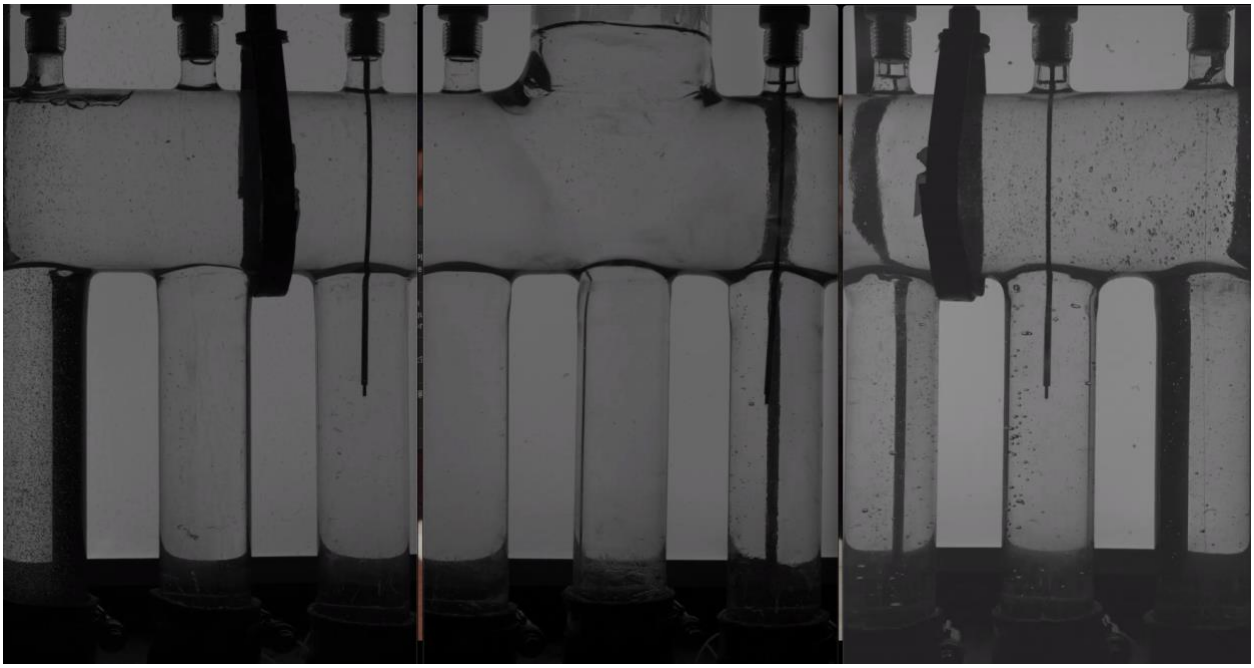

Figure 7.14: Boiling at Time 30

In Figure 7.13, the temperatures of the water when bulk boiling occurs, can be seen in all 9 risers. At time 0 seconds the temperature of all nine risers can be seen to be above or at saturation.

In Figure 7.15, the temperatures of the water when boiling can be seen for riser 8 positions 1-5 with the corresponding riser 8. In addition, in Figure 7.15, only the graph of the riser 8 positions 1-5 can be seen. Out of all the positions, position 5 of riser 8 had a higher temperature than all of the other positions, and is the last position to undergo cooling within the riser. This decrease in temperature occurs when the bubbles are quenched out of the riser, allowing for cooler water to flow into riser 8. As the reduction of temperature occurred, this caused the bubble size and bubble velocity to decrease. All of the positions in riser 8 have similar temperature profiles, but they are at different temperatures. In Figure 7.16, the risers 7 positions have a similar temperature profile of the riser 8 positions. However, the temperature in riser 7

decreases about 5 seconds after the temperature in riser 8. In Figure 7.17, the riser 6 positions have a different temperature profile when being compared to the temperatures in riser 7 and 8. This difference in the temperature profile demonstrates as risers 7 and 8 decrease in temperature, riser 6 is increasing in temperature and stay near saturation for a 15 second duration.

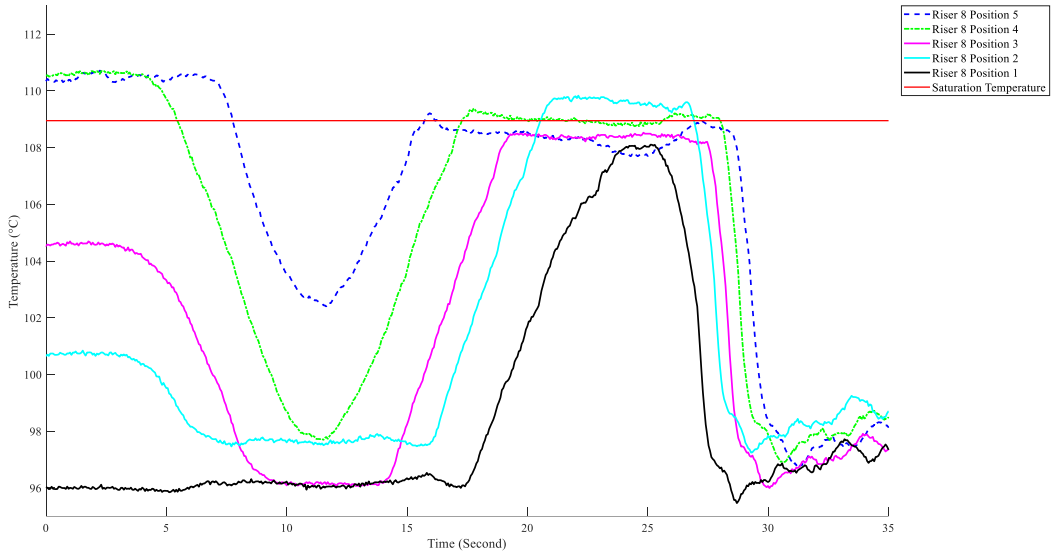

Figure 7.15: Boiling Temperatures of Positions 1-5 in Riser 8.

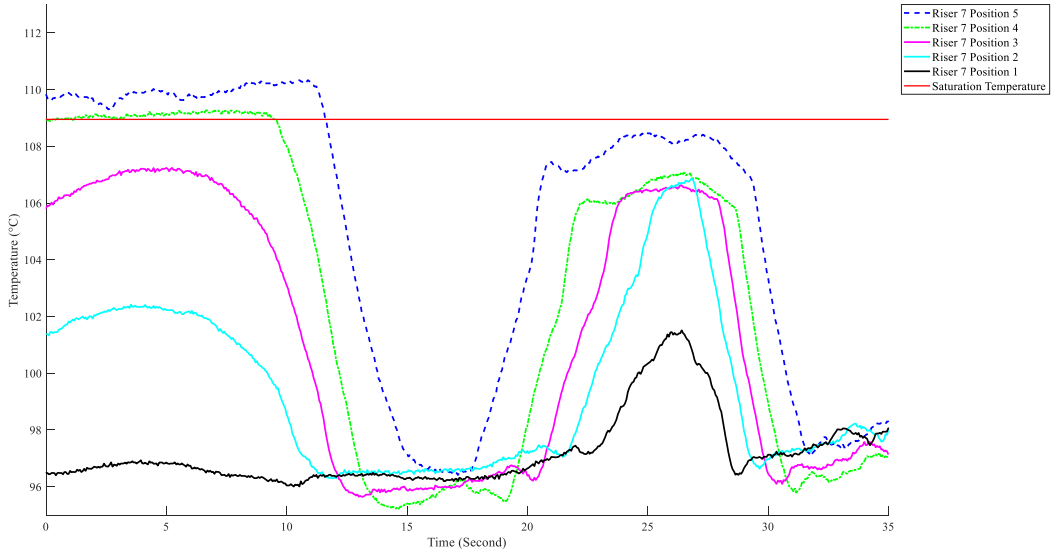

Figure 7.16: Boiling Temperatures of Positions 1-5 in Riser 7

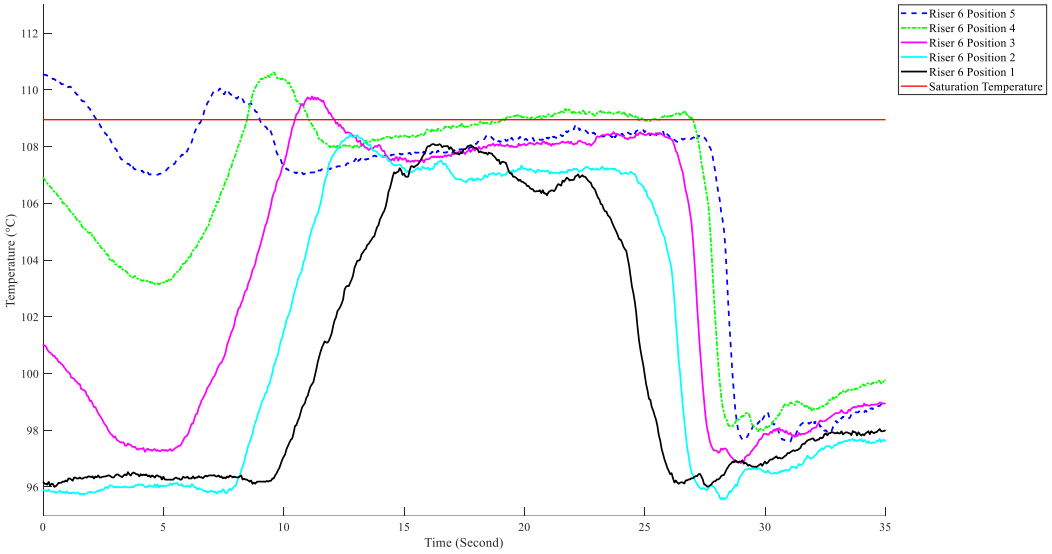

Figure 7. 17: Boiling Temperatures of Positions 1-5 in Riser 6

Finally, in Figure 7.18 which shows the riser 5 position, there is heating experienced just as seen in riser 6. Riser 5 and 6 have similarities in the temperature profile, however, the distinguishing factor is that riser 5 cools down 10 seconds before riser 6.

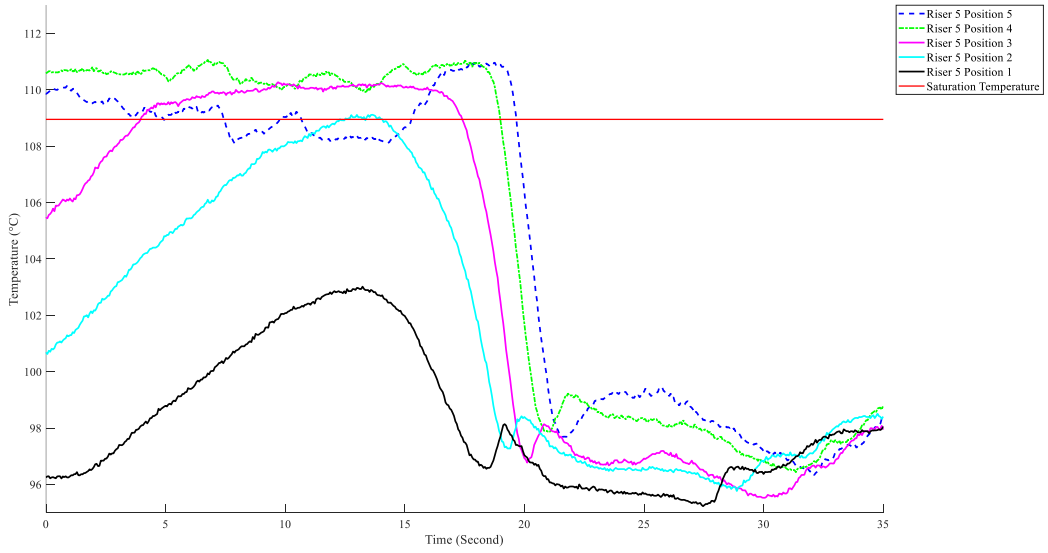

Figure 7.18: Boiling Temperatures of Positions 1-5 in Riser 5

7.7. Reverse Flow

After the riser boiling phenomena, the temperatures in the boiling riser start to decrease. As the temperature decreases, a phenomenon is observed. Figure 7.19 illustrates the start of riser 6's bubbles traveling the opposite direction of the original flow direction. While the bubbles in riser 6 travel downward, the remaining risers have bubbles that travel upward.

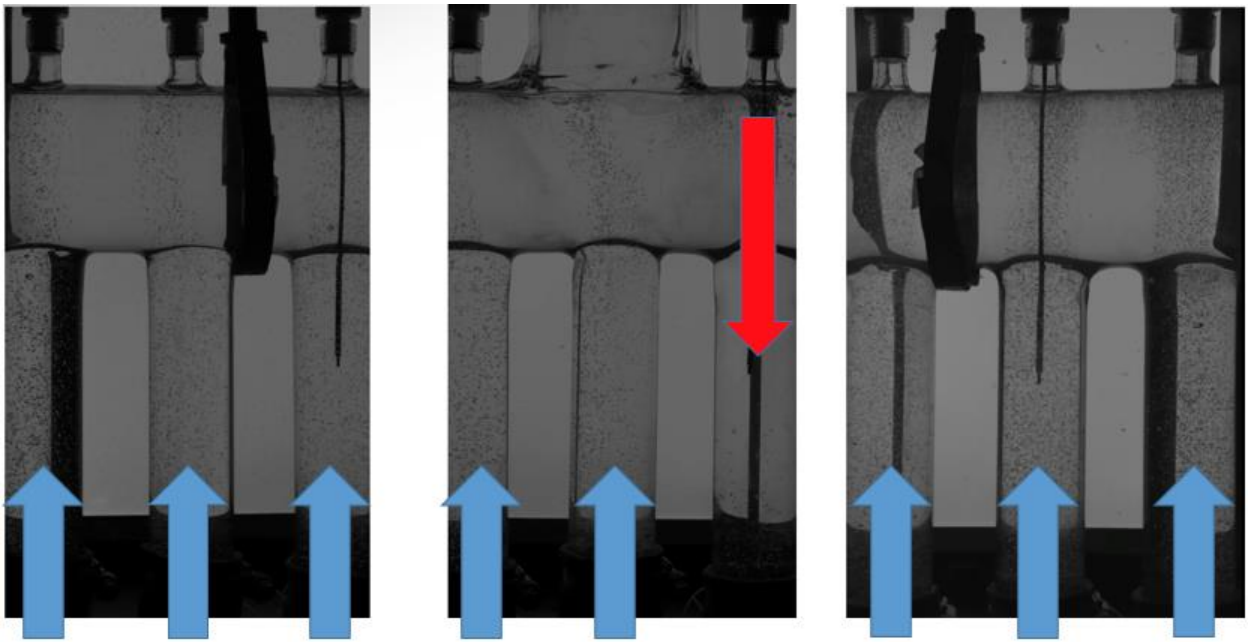

Figure 7.19: Reverse Flow in Riser 6 After Boiling

In Figure 7.20, an image of all of the risers was taken at 6 seconds and 9 seconds. The reverse flow temperatures all start above saturation temperature. At 6 seconds, only riser 6 experiences reverse flow. However, at another time riser 1 has been observed to experience reverse flow as well. As riser 6 decreases the temperature below the saturation temperature, the bubble velocity increases in the downward direction.

In Figure 7.21, the position of the bubble in riser 6 can be seen to be at the top of the transparent glass upper manifold. Yet as shown in Figure 7.22, the position of the bubble in riser 6 can also be seen to be in the middle of the transparent glass upper manifold. This occurs until 12 seconds where the temperature decreases to 107 degrees Celsius. Once the temperature in riser 6 decreases to 107 degrees Celsius, the bubbles continue to travel downward as the velocity decreases. As the temperature starts to increase to 108 degrees Celsius, the bubbles continue to travel downward a velocity nearing 0 m/s until 12 seconds where the bubbles begin to travel in the upward direction. Furthermore, the temperatures for all the risers at the highest position was displayed in Figure 7.23. This graph depicts that riser 6 is the coldest riser when the flow reversal occurs.

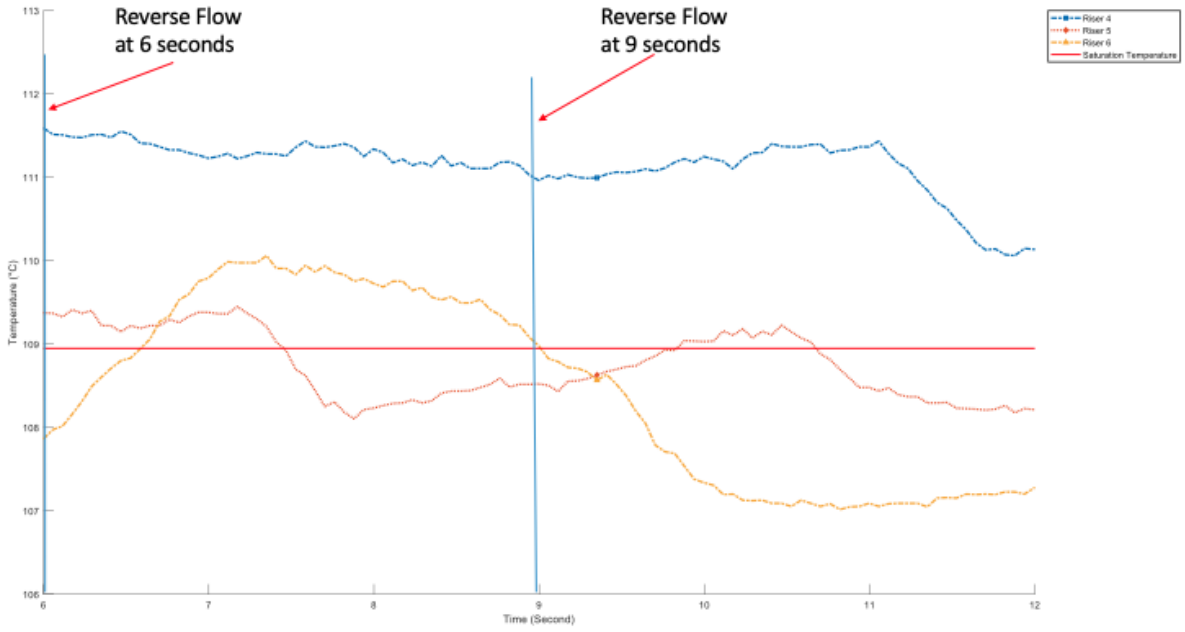

Figure 7. 20: Reverse Flow Temperatures in Riser 4, 5, and 6

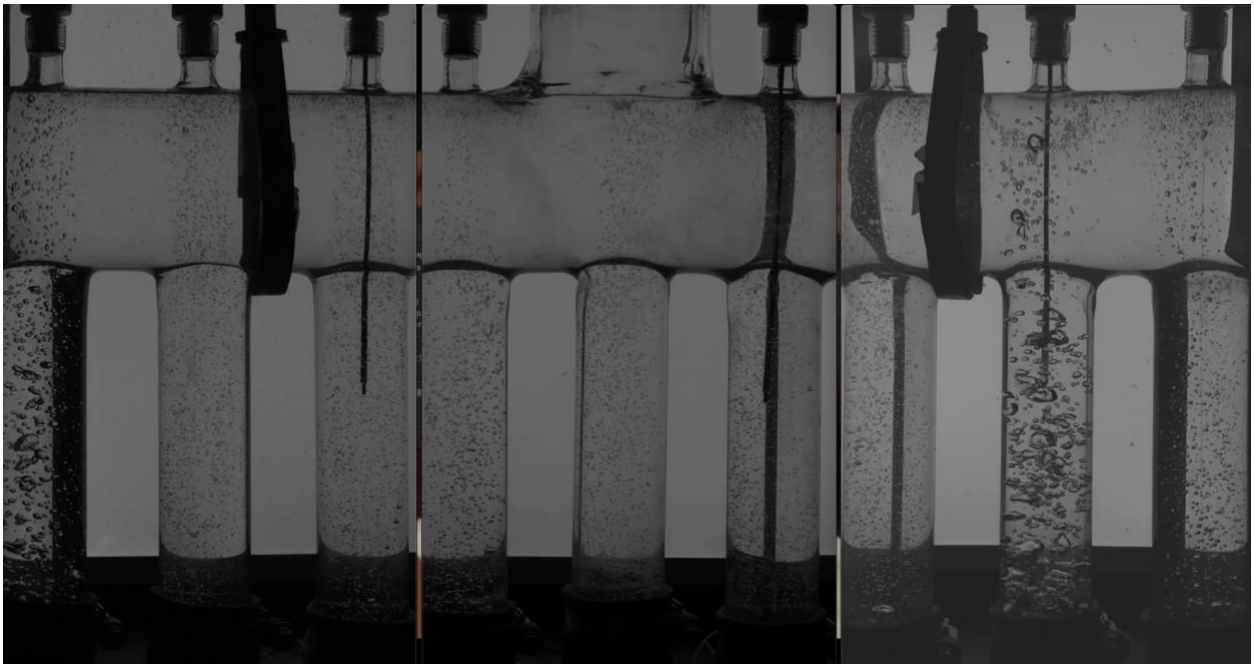

Figure 7.21: Reverse Flow at Time 6

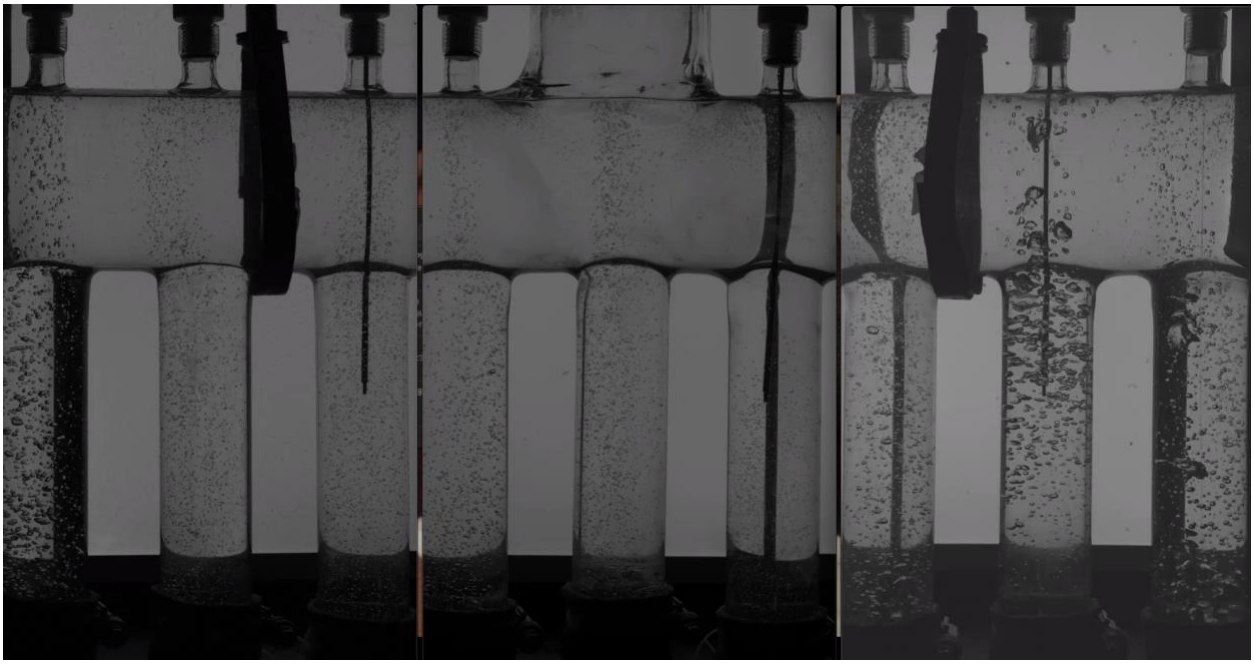

Figure 7.22: Reverse Flow at Time 9

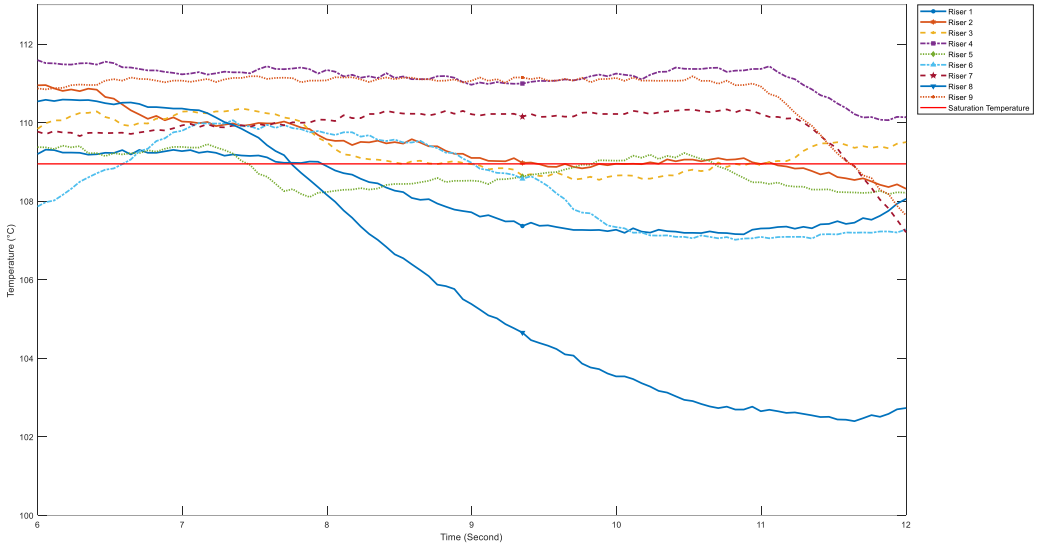

Figure 7.23: Reverse Flow Temperatures of All Risers.

In Figure 7.24, the temperatures of the water when boiling can be seen for riser 6 positions 1-5 with the corresponding riser 6. At 6 seconds, the small bubbles can be seen in riser 6. The vapor density is less dense when compared to the other risers. At 6 seconds, riser position 1 and position 5 have a difference in temperature of 13 degrees Celsius. In addition, position 2 is 1 degree Celsius cooler than position 1. At time 6, position 5 starts to decrease in temperature while the other positions start to increase in temperature. The temperature of position 5 decreases in temperature and the other positions increase in temperature until the riser 2-5 are 1 to 2 degrees below saturation temperature of water. A reduction in temperature could be related to a pressure difference that causes the bubbles to travel in the opposite direction. In addition, Figure 7.25 displays temperatures of the water when boiling can be seen for riser 5 positions 1-5.

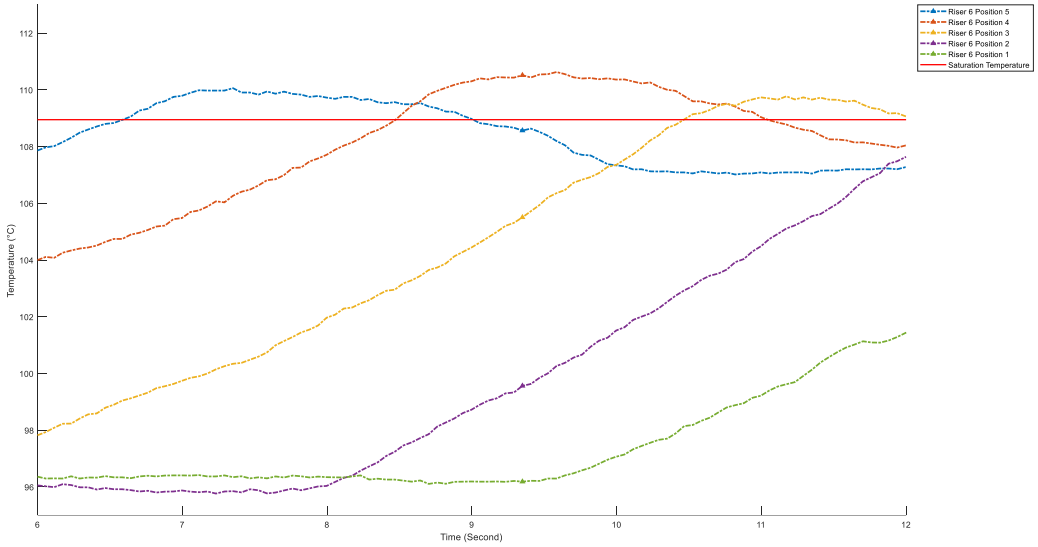

Figure 7.24: Reverse Flow Temperatures of Positions 1-5 in Riser 6.

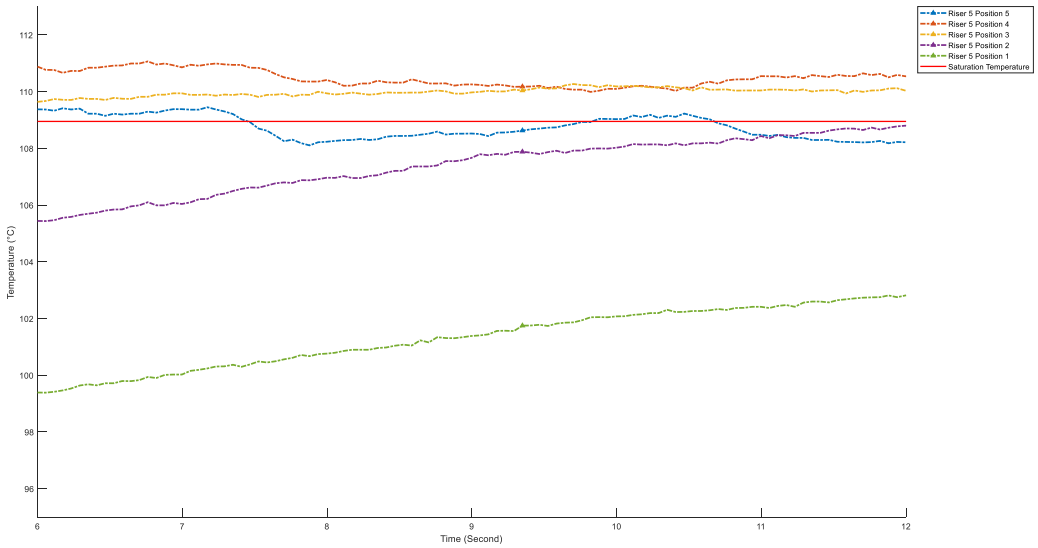

Figure 7.25: Reverse Flow Temperatures of Positions 1-5 in Riser 5.

7.8. Tank Valve 25% Open

After conducting the experiments above with the tank valve 100% open, a test was conducted with the tank valve 25% open. Figure 7.26 shows the boiling velocity of air increasing, which causes the RCCS to experience a slug flow with large pockets of air. This RCCS slug flow was only experienced when the tank valve was at 25%. This phenomenon could have occurred due to the water traveling at a low flowrate, causing the water to be in contact with the three 8kW heaters for a longer duration than if the tank valve was 100% open. Allowing the water to contact the heaters for a longer duration caused more heat to be transferred to the water than if the heaters had less time to transfer heat to the water. When more heat is transferred to the water, the temperature of the water increases to a temperature that was not achieved when the tank valve was 100% open.

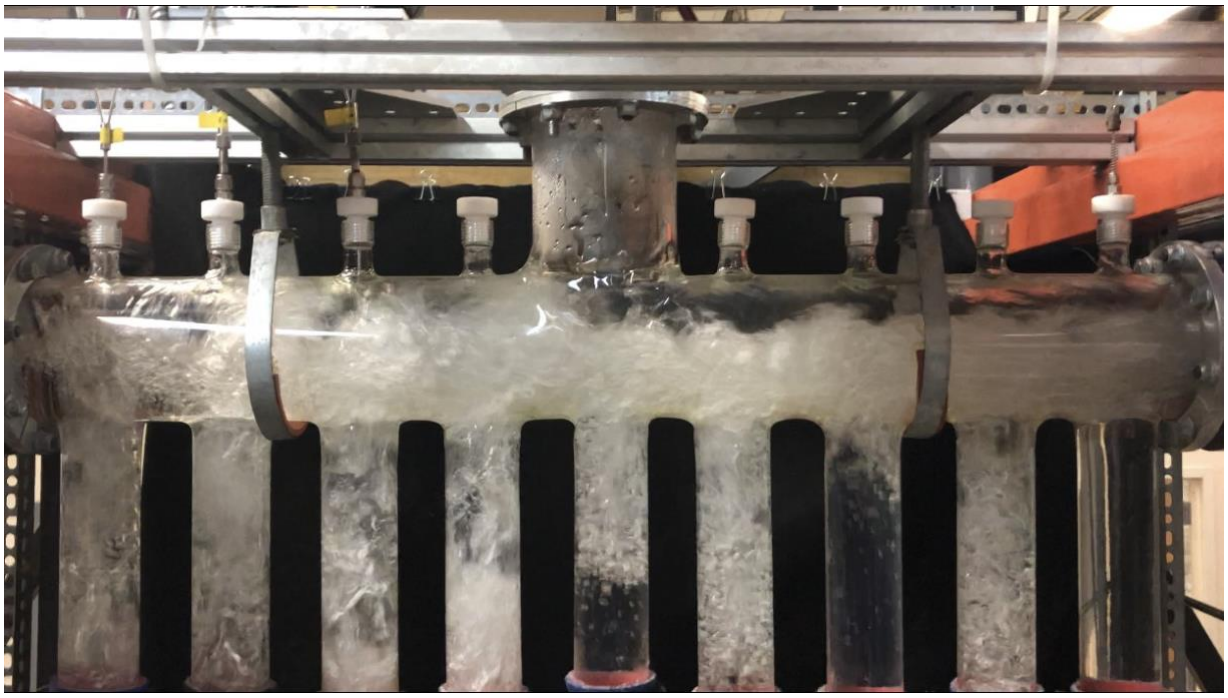

Figure 7.26: Slug Flow with Tank Valve at 25% Open on the RCCS

8. CONCLUSION

8.1. Summary

Two-phase flow is asymmetric in the bubbly regime in the RCCS. Also, two-phase flow measurements are not feasible with the probes in the RCCS due to bubble size and velocity. The bubbles are too small and do not travel in a straight trajectory; and they are not intersected by the two tips, thus inducing poorly correlated signals. Furthermore, two-phase bubbly flow must have a more powerful chiller that can keep the RCCS at a stable bubbly flow regime for over an hour. Once bulk boiling is established there are instabilities in the two-phase flow. These instabilities cause changes in the flowrate of water, velocity of the bubbles, and temperature of the water. Also, changing the flowrate of water dictated by the tank valve position changes the two-phase phenomena observed. Finally, the recommendation is to continue two-phase flow and pressure measurements in the RCCS for future research studies.

8.2. Future Work

Two-phase measurements can be continued once a steady state at bubbly flow regime can be achieved in the RCCS. Having two-phase measurements will be beneficial to correlate the void fraction with temperature. In addition, two-phase measurements on a different flow regime can be studied to observe flow behavior changes. Observing different regimes will allow for a better characterization of the two-phase flow progression as longer acquisition times become achievable. Moreover, investigating the two-phase flow behaviors as tank valve positions change will allow for a better understanding of how the flowrate of water has an effect of the velocity of the bubbles as bubbly flow is established in the RCCS. Additionally, PTV can be performed

using images to correlate bubble velocity as a function of time. This will help quantify the difference in velocity between all of the nine risers. Finally, void fraction can be calculated as a function of temperature in order to further quantify the temperature of the RCCS when a bubbly flow or slug flow is established.

REFERENCES

Benjamin, T. B. (1968). Gravity currents and related phenomena. *Journal of Fluid Mechanics*, 209-248.

Conklin, J. (1990). *Modeling and Performance of the MHTGR Reactor Cavity Cooling System.* Oak Ridge: U.S. Nuclear Regulatory Commision.

Corradini, M. (2012). *Experimental Studies of NGNP Recator Cavity Cooling System with Water.* University of Wisconsin - Madison, Nuclear Engineering. Madison: U.S. Department of Energy.

Godbole, P. V., Tang, C. C., & Ghajar, A. J. (2011). Comparison of Void Fraction Correlations for Different Flow Patterns in Upward Vertical Two-phase Flow. *Heat transfer engineering*, 18.

Gouzhi, Z., Xinrong, C., & Xingwei, S. (2013). A Study Using RELAP5 on Capability and Instability of Two-phase Natural Circulation Flow Under Passive External Reactor Vessel Cooling. *Annals of Nuclear Energy*, 12.

Hassan, Y. (2013). *CFD Model Development and Validation for High Temperature Gas Cooled Reactor Cavity Cooling System Applications.* Texas A&M University, Nuclear Engineering. College Station: U.S. Department of Energy.

Krueger, A. M. (2016). Uncertainty Quantification by Monte Carlo Analysis using CFD Simulations for GEMIX Benchmark Activities. *Transactions of the American Nuclear Society*, 1744-1746.

Lisowski, D., Omotowa, O., Muci, M., Tokuhiro, A., Anderson, M., & Corradini, M. (2013). Influences of Boil-off on the Behavior of a Two-phase Natural Circulation Loop. *International Journal of Multiphase Flow*, 14.

Obabko, A. V. (2012). Large Eddy Simulation of Thermo-Hydraulic Mixing in a T-Junction. . *InTech*.

Park, R., Ha, K., Kim, S., & Kim, H. (2006). Two-phase Natural Circulation Flow of Air and Water in a Reactor Cavity Model Under an External Vessel Cooling During a Severe Accident. *Nuclear Engineering and Design*, 7.

RBI. (2005). *ISO Software User's Guide.* Meylan, France: RBI.

Tompkins, C. A. (2017). *Experimental Investigations in a Reactor Cavity Cooling System with Advanced Instrumentations for the Study of Instavilities, Oscillations, and Transients.* University of Wisconsin - Madison, Nuclear Engineering. Madison: University of Wisconsin - Madison.

Tompkins, C., & Corradini, M. (2018). Flow Pattern Transition Instabilities in a Natural Circulation Cooling Facility. *Nuclear Engineering and Design*, 12.

Tompkins, C., & Corradini, M. (2018). *Water-cooled Reactor Cavity Cooling System Flow Analysis.* University of Wisconsin - Madison, Nuclear Engineering. Madison: Uiversity of Wiscosin - Madison.

Vaghetto, R. (2013). *Experimental and Computational Study of a Scaled Reactor.* Texas A&M University, Nuclear Engineering. College Station: Texas A&M University.

Vaghetto, R., & Hassan, Y. A. (2014). *Experimental Investigation of a Scaled Water-Cooled Reactor Cavity Cooling System.* College Station: Nuclear Technology.

Woldesemayat, M. A. (2006). *Comparison of Void Fraction Correlations for Two-phase Flow in Horizontal and Upward Inclined Flows.* Oklahoma: Oklahoma State University.

APPENDIX

A.1. Section A: ISO Software Guide

When opening the ISO software, the user will be directed to the main menu as seen in Figure A.1. In the main menu, geometry is needed to correctly establish a distance between the sapphire tips. When clicking the probe geometry and location, the user will be directed to the probe geometry window (Figure A.2). In this window, the longest tip of the sapphire tips is considered the point of origin. For sensor 0, the x, y, and z parameters are all 0. The e parameter associated with each probe is the distance between the sapphire tips. This distance is used when inputting the geometry of the second sapphire tip. For sensor 1, the x and y parameters are 0 in the probe geometry window, and the z parameter is equal to the e parameter of the corresponding probe. When setting up the second and third probe, repeat the same steps for sensors 2 and 3 and sensors 4 and 5. Click validate to be directed back to the main menu.

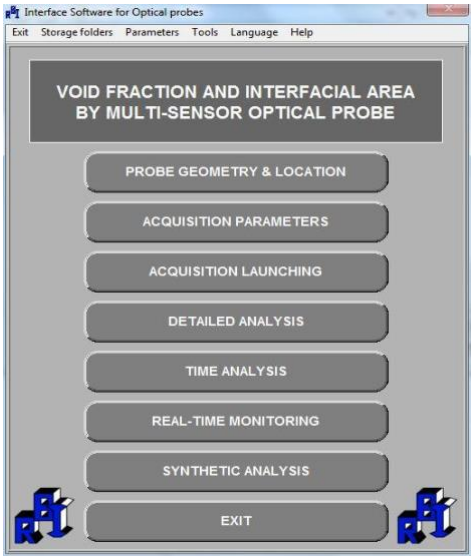

Figure A.1: Main Menu of the ISO Software (RBI, 2005)

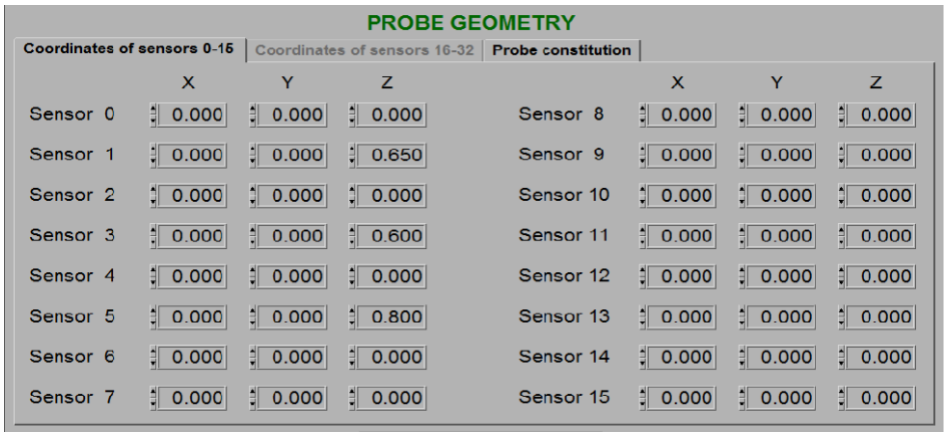

Figure A.2: Probe Geometry (RBI, 2005)

When clicking the acquisition parameters, the user will be directed to the setting of acquisition parameters window as seen in Figure A.3. Next, activate the probe by selecting both the corresponding sensors. Up to six sensors can be selected. In addition, a bubble number limit has to be set as a condition run the acquisition. The bubble number should be set higher than the desired number of bubbles received by the probe. Set the average void fraction plot during acquisition to 10 seconds or less. Set the operating mode master to allow the acquisition to run after clicking the acquisition launching in the main menu. After that, save the acquisition time by clicking validate, and then the user will be directed to the main menu. The acquisition can be started by clicking acquisition launching in the main menu. Save the data on the computer.

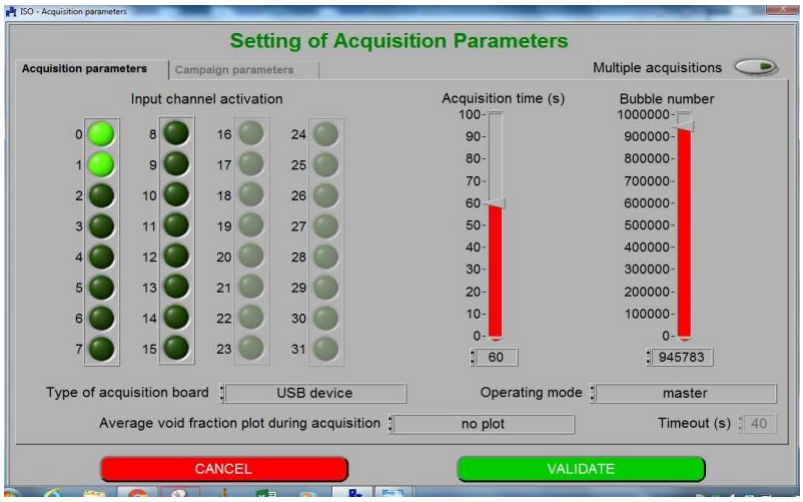

Figure A.3: Setting of the Acquisition Parameters (RBI, 2005)

By clicking a detailed analysis in the main menu, the user will be directed to choose a saved file on the computer as seen in Figure A.4. Then the detailed analysis window will appear. In the detailed analysis menu, the user can select the signal visualization. The user will be directed to the signal visualization window (Figure A.5). In this window the user can see the individual signals for each sensor. Also in this window, the user can select an individual signal or up to six signals simultaneously.

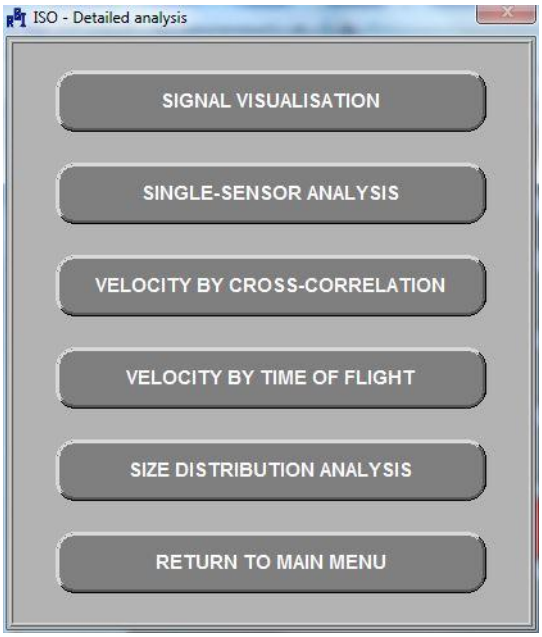

Figure A.4: Detailed Analysis Menu (RBI, 2005)

Figure A.5: Signal Visualization (RBI, 2005)

In the detailed analysis menu, the user can further select the single-sensor analysis, which will direct the user to the phase time histogram window as shown in Figure A.6. In the histogram, the user can see the population of bubbles that correspond to the time the sensors

detected bubbles. The same can be said for the liquid histogram. The population of liquids corresponds to the time the sensors detected liquid. Also, this window displays the acquisition time the probes measured for, the calculated void fraction, and the total bubble number based off the gas histogram. To return back to the detailed analysis menu, click the stop button.

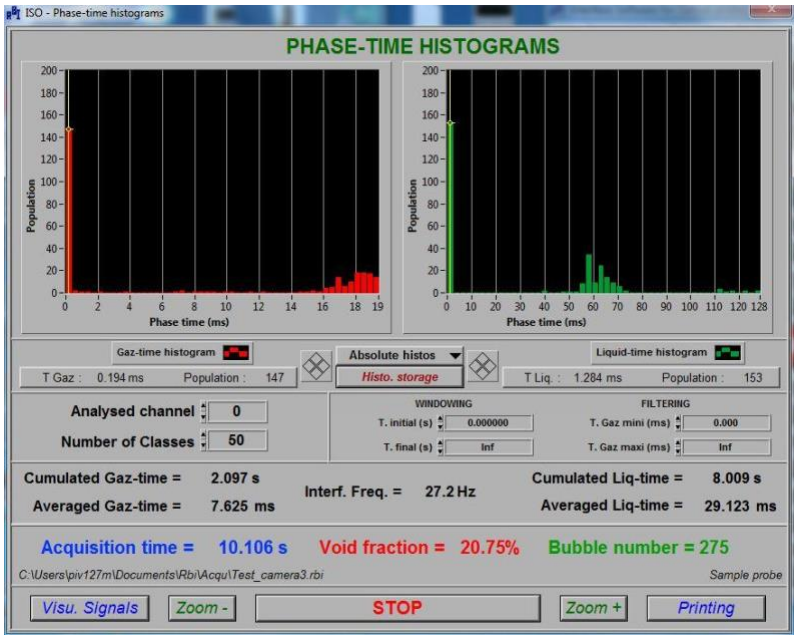

Figure A.6: Single-Sensor Analysis (RBI, 2005)

In the detailed analysis menu, the user can select the velocity by cross-correlation, which will direct the user to the cross-correlation analysis window (Figure A.7). In this window, the user can see the correlation coefficient as the time of flight changes. The max value of this graph is the time of flight value that corresponds with the analysis. As a consequence, this window shows the calculated velocity based on the distance between the tips divided by the time of flight. In addition, the peak of correlation and both coefficients A_i and D_{sm} are displayed in this window. To return back to the detailed analysis menu, click the stop button.

In the detailed analysis menu, the user can select the velocity by time of flight, which will direct the user to the time of flight histogram window as depicted in Figure A.8. In this window, the user can see the population as the time of flight changes for both the rising and falling edges. Further displayed in this window is the calculated velocity, time of flight, and both coefficients A_i and D_{sm}. This shows the rising and falling edges. To return back to the detailed analysis menu, click the stop button.

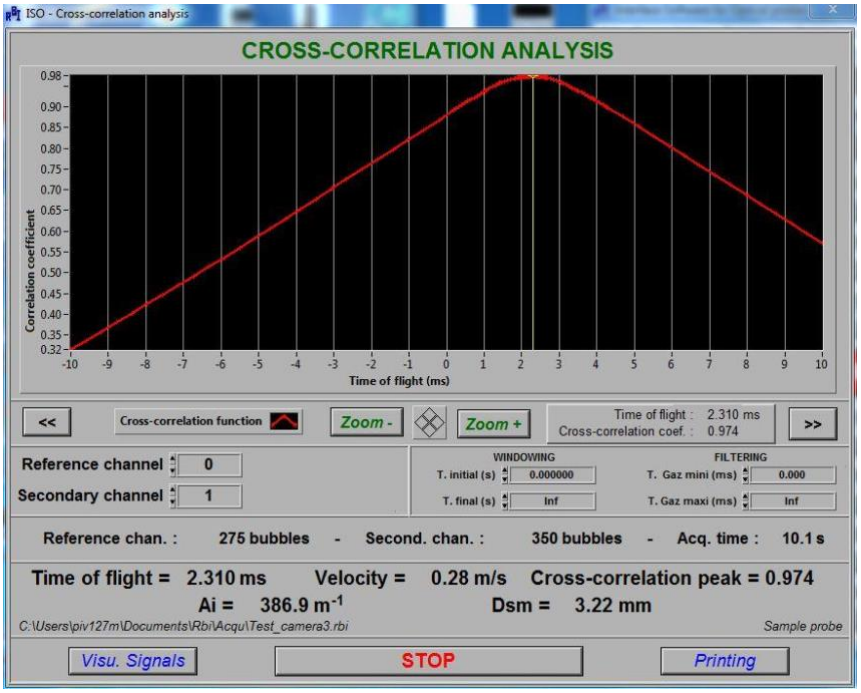

Figure A.7: Velocity by Cross-Correlation (RBI, 2005)

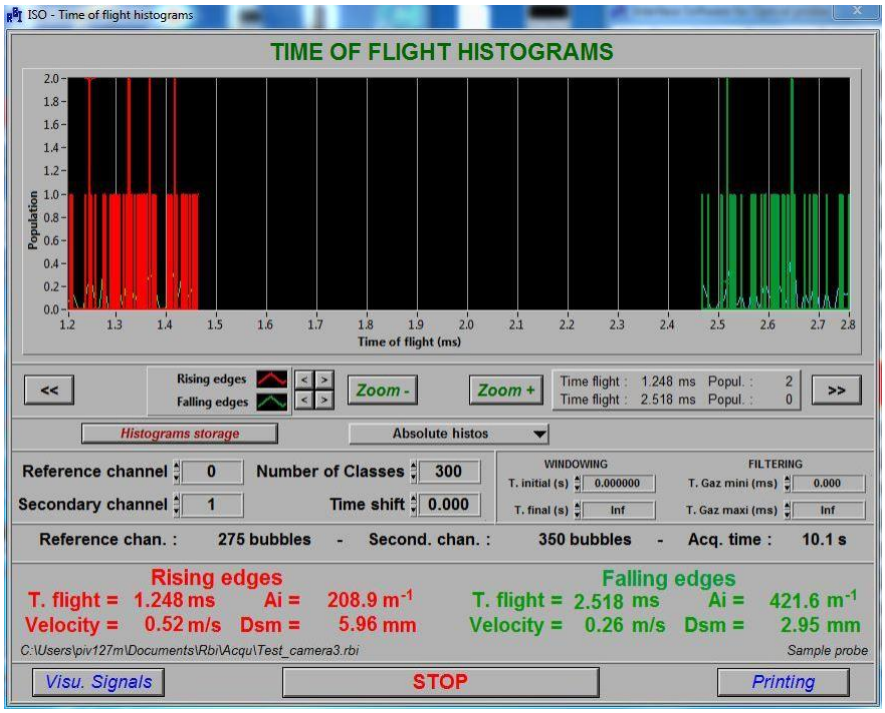

Figure A.8: Velocity by Time of Flight (RBI, 2005)

In the detailed analysis menu, the user can select the size distribution analysis which will direct the user to the bubble size distribution window as seen in Figure A.9. In the window, the user can see the bubble population as it progresses through the sapphire sensor length which also corresponds to the bubble size. This window also shows the calculated velocity and both coefficients A_i and D_{sm}. To return back to the detailed analysis menu, click the stop button. To be directed back to the main menu, click return to main menu.

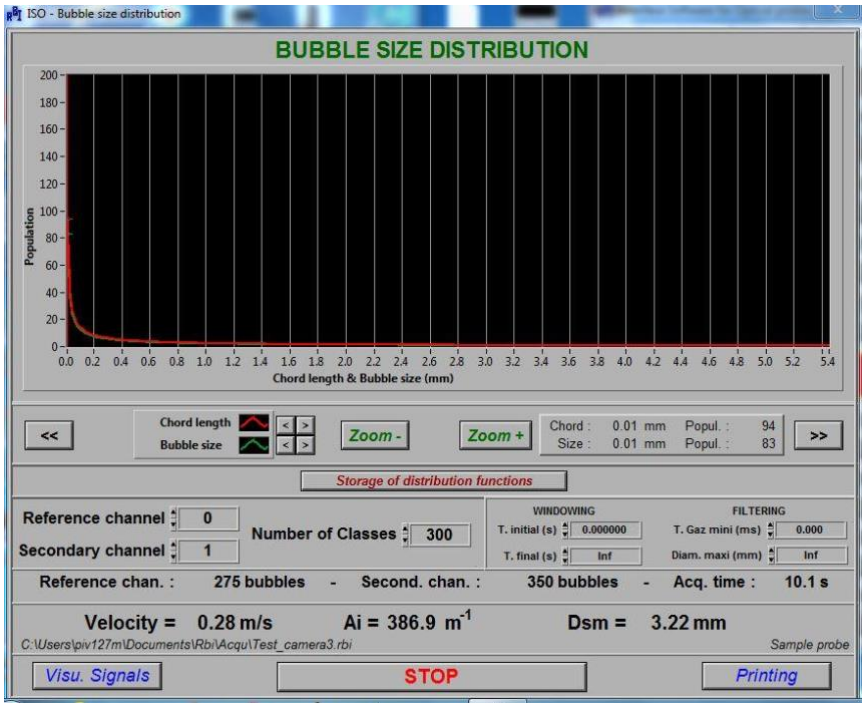

Figure A.9: Size Distribution Analysis (RBI, 2005)

Once in the main menu, select real-time monitoring which will direct the user to the phase time histogram window. In the histogram window, the user can see the population of bubbles that correspond to the time the sensors detected bubbles. The same can be said for the liquid histogram. The population of liquid corresponds to the time the sensors detected the liquid. Also, the display in this window reflects the acquisition time the probes measured for, the calculated void fraction, and the total bubble number based off the gas histogram. These parameters are calculated every two seconds to monitor the real-time fluctuations. To return back to the main menu, click the stop button.

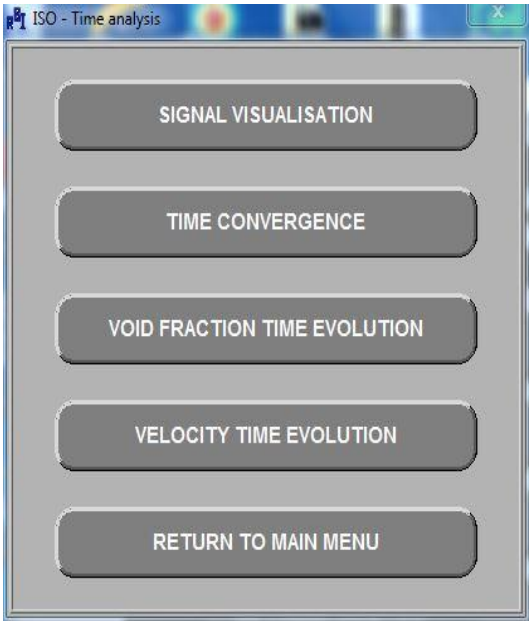

Figure A.10: Time Analysis Menu (RBI, 2005)

Once in the main menu, select synthetic analysis which will direct the user to the synthetic analysis window after the acquisition file is selected as seen in Figure A.10. In the synthetic analysis window, the user can see the calculated void fraction that correspond to each individual sensor. Only one probe or two sensors can be viewed simultaneously. To return back to the main menu, click the stop button. In addition, the main menu allows access to the time analysis feature. By clicking on time analysis, the user will be directed to the time analysis menu after choosing a data file saved on the computer. In this window, the user can view the change in velocity over time and the change in void fraction over time. By selecting the time convergence in the time analysis menu, the user can see the void fraction over time and the bubble population over time as well. To return to the main menu, click return to main menu.